Report on a problem studied at the UK Mathematics-in-Medicine Study Group Southampton 2007
< https://mmsg.mathmos.net/uk/2007/tissue-printing/ >

7TH MATHEMATICS IN MEDICINE STUDY GROUP
UNIVERSITY OF SOUTHAMPTON, 10–14 SEPTEMBER 2007

Regenerative Medicine Using Organ Printing Technologies

Study Group contributors

Ovidiu Bagdasar (University of Nottingham)
Clare Bailey (University of Loughborough)
Rebecca Carter (University of Oxford)
Chris Catt (University of Southampton)
Louise Dyson (University of Oxford)
Rosemary Dyson (University of Nottingham)
Liesbet Geris (K. U. Leuven)
Gareth Jones (University of Oxford)
Kerry Landman (University of Melbourne)
Jonathan Moles (University of Southampton)
Colin Please (University of Southampton)
Sylvain Reboux (University of Nottingham)
Tiina Roose (Universities of Oxford and Southampton)
Zimei Rong (Queen Mary University of London)
Bram Sengers (University of Southampton)
Muhammad Shakeel (University of Nottingham)

Report Prepared by

Rebecca Carter (University of Oxford) Liesbet Geris (K. U. Leuven)
Sylvain Reboux (University of Nottingham)

Problem presented by

Jos Malda, University of Utrecht

Problem Statement

Cartilage tissue repair procedures currently under development aim to create a "construct" that can be grown in a bio-reactor and that mimics the real tissue. The construct can consist of a scaffold made of strands of material that are set out into a 3D structure using printing technology. The material (a hydrogel/biomaterial mix) consists of a gel to provide mechanical stability and a template for the delivery of cells that create cartilaginous tissue. For a relatively complex tissue such as cartilage, it may be necessary to construct a layered structure with the strands of material (containing different cells) having different sizes and orientations at different places. The Study Group was asked to determine practical design criteria for the construct structure and bioreactor design that ensure that the cells in the construct create a suitable distribution of cartilage. After the meeting, constructs will be manufactured and cultured in vitro based on the outcomes of the MMSG and the experimental results obtained will be communicated back to the mathematicians.

1 Introduction

The purpose of tissue engineering is the design and fabrication of constructs to replace degenerated or diseased tissue. The two main focuses are engineering nonvascularized and vascularized tissues. Conventional tissue engineering is directed at nonvascularized tissue where it is hoped that regeneration of cartilage, bone, tendons and intervertebral discs using tissue engineering will offer a source for the increasing demand for these tissues in an aging population. Tissue engineering for this application involves seeding porous, biodegradable scaffold materials with chondrocytes (cartilage-producing cells) (for examples of scaffolds see Figure (1)). The scaffold is then incubated in a bioreactor for several weeks to allow the cells to grow into the pores before being surgically implanted into the patient where, depending on the tissue, angiogenesis occurs to provide permanent vascularization and the scaffold degrades and is replaced with extracellular materials such as collagen and proteoglycans. These conventional strategies have also been applied to organ printing for heavily vascularized tissues such as the kidneys and liver, motivated by an increasing shortage of donor organs. However, this was with limited success and consequently further designs have been developed to incorporate designs of microvascular networks based on branching systems in living organisms with novel microfabrication technologies to produce biocompatible and biodegradable microfluidic channels [3, 6].

Body tissue is a highly organised structure made up of cells and extracellular matrix, and the fabrication of replacement tissue should mimic this spatial organization. For example, within natural cartilage cell density varies slowly with depth, and ideally this should be mimicked in a tissue-engineered construct (see Figure (2)). However, currently the quality of the implants falls short of that of the native tissue. One limitation is ensuring adequate nutrient delivery and waste disposal to each of the cells in the scaffold, and to date little research has been directed at understanding this problem. The nu-

trients required by the cells include oxygen and glucose, and these are delivered to the cells via a liquid called a culture medium. The cells use these nutrients in respiration to proliferate and produce waste products such as lactate as a consequence. Lactate is acidic and so lowers the pH of the culture medium, which has the effect of decreasing cell proliferation rates and viability. Therefore it is extremely important both to provide adequate nutrients to the cells, and remove waste products from the system.

Central questions for the design are:

- What is the best size and layout for the strands within the construct for good flow and nutrient transport while creating cartilage quickly?
- How can the design be modified to avoid regions of low cartilage growth or low nutrient?
- How quickly can the nutrients be pushed through the construct without significantly deforming or damaging the structure?
- How will the cartilage tissue components that are produced by individual cells form an integrated, functional, cartilage matrix (see Figure (3)) ?

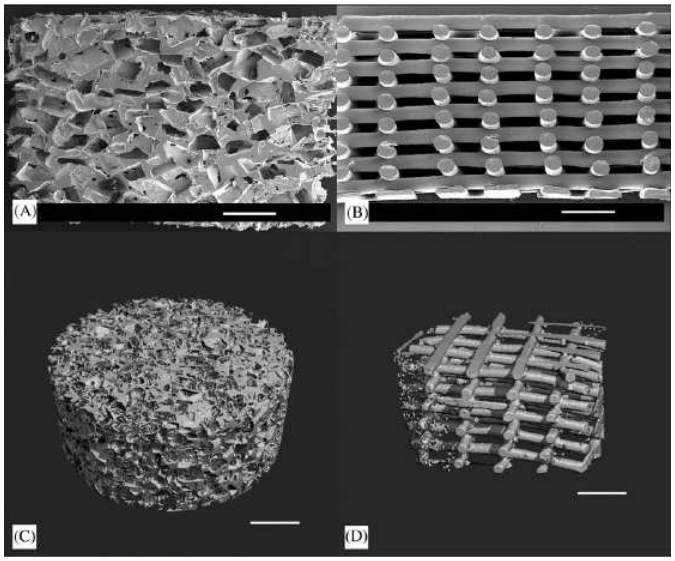

Figure 1: Electron micrographs of CM (A) and 3DF (B) scaffolds. Three-dimensional reconstruction of CM (C) and 3DF (D) scaffolds from μCT scans. Scale bar represents 1 mm. Reproduced from [11].

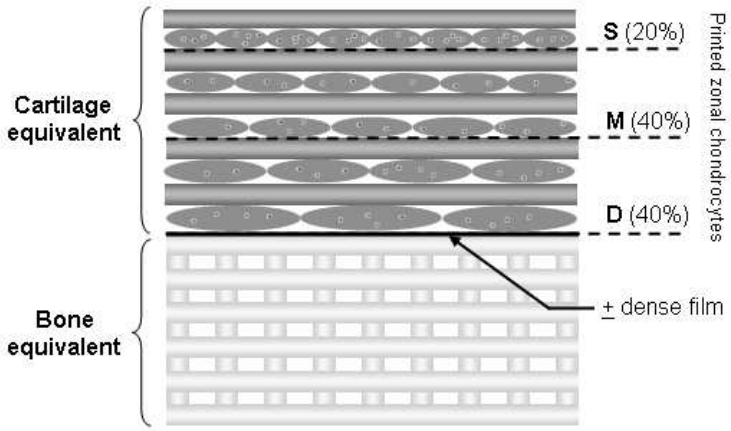

Figure 2: A comparison of natural cartilage with the tissue-engineered equivalent.

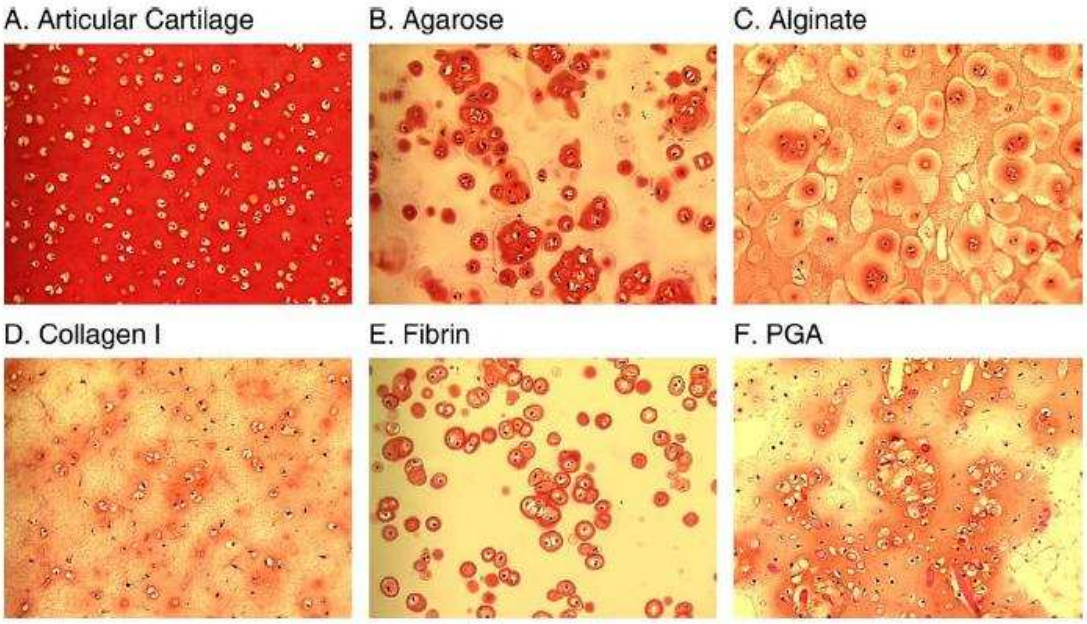

Figure 3: Representative sections of cartilage (A) and tissue engineered constructs cultured for 20 days, using different construct materials (B-F). Sections have been stained with Safranin-O (red) to show the deposition pattern around the cells of proteoglycans, one of the main components of the cartilage extracellular matrix. Reproduced from [5].

During the MMSG, the group separated into subgroups which worked on various aspects of the project. These are reported in the following sections, and the notation in each section is entirely self-contained. §2 discusses the structure of the construct. §3 considers the mechanical aspects of the problem, starting by calculating the stresses on an individual strand and then extending these results to the whole scaffold and finding the maximum fluid velocity that can be withstood by the structure. In §4 we model the growth of the extracellular matrix (ECM) by considering a single spherical cell that produces matrix elements which diffuse into an homogenous, isotropic medium and bind with each other to form the ECM. Finally in §5 we consider the fluid flow and oxygen transport problems, starting from a single strand setup and finally extending this by homogenization to a multiple strand scaffold.

2 Structure

In this section we discuss the structure of the scaffold and possible improvements that could be implemented in future constructions. The hydrogel is extruded at constant flux to form a three dimensional construct made up of layers of rod-like structures. Typically constructs have height 2mm, and gel strand diameter $\approx 200\mu$m, similar to the structures shown in Figure (1). The cartilage consists of three distinct layers, each containing a different type of cell. Therefore, each layer of the construct is printed using a different gel. The initial surface of the printed tissue is about $10mm^2$. The original method was to build the scaffold on a plate (see Figure (4)) and to force the fluid through the construct from one side. To provide some additional strength to the structure, the direction of the rods from one layer differs from the direction of the rods in the following one by an angle of 90°. One improvement would be to force the fluid through the construct from the top, as shown in Figure (5). A second would be to replace the plate on which the scaffold is built with a grid of the same shape. Since the cartilage is grown within the skeleton of the printed grid, the growing structure will also allow the vertical flow. Passing the flow "top down" also removes any restriction on the cross sectional area of the produced tissue; we merely have a restriction on the thickness of the cartilage produced.

The volume fraction of the structure was also considered during the MMSG. A larger volume fraction will allow for more cartilage development which is clearly beneficial (providing there are no detrimental effects for nutrient/waste product transport). We consider the setup shown in Figure (5) and let a be the strand separation and r be the

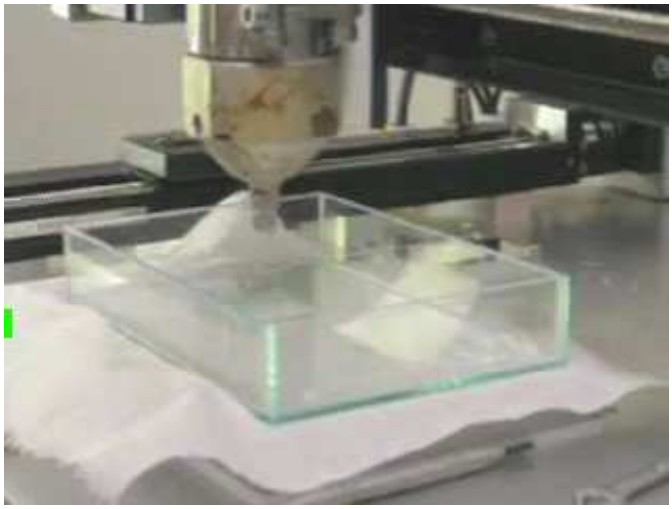

Figure 4: The apparatus used to build the scaffold

strand radius. The volume fraction of the structure is then given by

$$V_f = \frac{\pi}{2(2 + \frac{a}{r})}. \tag{1}$$

For example, in the special case $a = 2r$, $V_f \approx 0.39$. Moreover, the spaces between the rods in one layer which have some rod of the previous layer laying under them can be filled with some drop of gel. The increase of volume is of the order of 50%, so we obtain $V_f \approx 0.60$.

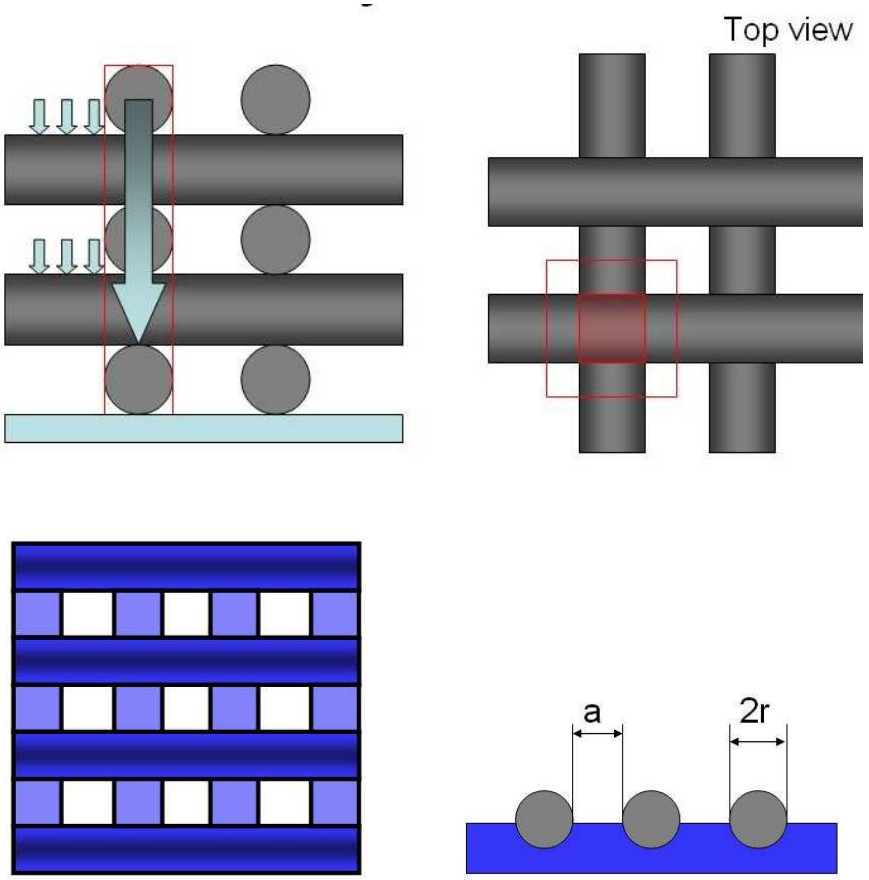

Figure 5: Top: A possible scaffold structure. Bottom: The corresponding lattice structure.

3 Mechanical aspects

3.1 Force generated by fluid flow

Koch and Ladd [7] described the relation between the mean drag and the solid volume fraction of an array of cylinders for very small Reynolds numbers. For the solid volume fraction corresponding to our scaffold ($\phi = 0.4$, inter-fibre spacing equal to diameter), this resulted in

$$\frac{F}{\mu v} \simeq 10^2 \tag{2}$$

with F being the drag force per unit length acting on the cylinders, μ the fluid viscosity and v the velocity. For $\mu = 7 \cdot 10^{-4}$kg m^{-1} s^{-1} (water 37°C), this leads to the following relation between the drag force on the cylinders and the fluid velocity:

$$F = 0.07v. \tag{3}$$

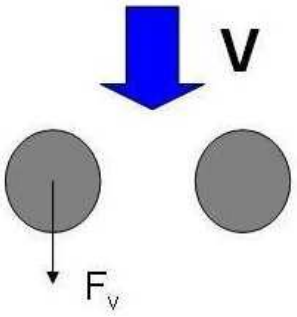

Figure 6: Fluid flow through an array of cylinders

3.2 Behaviour of individual struts

For the investigation of the behaviour of an individual strut, we considered a simply supported beam (Figure (7)) and calculated the maximal fluid velocity that would generate tensile and shear stresses within the limits of the material and a considerable displacement of the strut.

- The maximum tensile stress in a simply supported beam is given by the formula

$$\sigma_{max} = \left| \frac{pL^2}{8z} \right|. \tag{4}$$

  Here p represents the load per unit length ($p = F$ derived in the previous section), L the distance between the supports, $z = I/c$ where c is the distance from the neutral axis to the extreme fibers and I the moment of inertia. The moment of

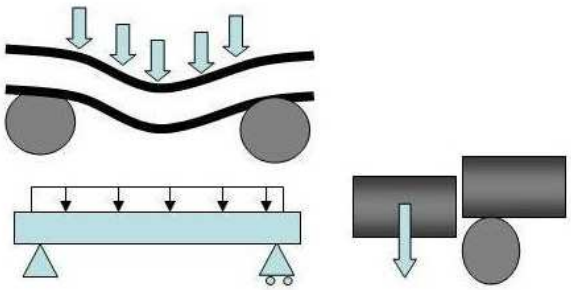

Figure 7: Simply supported beam. Left: deformation under distributed load. Right: shear stress.

inertia (second moment of area) for a cylindrical beam is given by $I = \pi D^4/64$ with D the diameter of the beam. For this problem we get: $p = 0.07v, \quad D = 200\mu m, \quad L = 400\mu m, \quad c = 100\mu m$. As various (quite large) values of maximal tensile stress are reported for alginate in literature, we derived the maximal tensile stress based on the Young's modulus allowing a 10 % deformation. For a Young's modulus of 20 kPa [1], this gives us a maximal tensile stress of 2 kPa. From this we can calculate the maximal allowed fluid velocity: $v_{max} = 1.1\text{m s}^{-1} = O(1)\text{m s}^{-1}$.

- The maximum shear stress in a simply supported beam is given by the formula

$$\tau_{max} = \left| \frac{T_{max}}{A} \right|, \tag{5}$$

where A is the cross section of the strut. T_{max} represents the maximal shearing force exerted on the strut. This maximal shearing force is found at the ends of the strut as indicated in Figure (7): $T_{max} = pL/2$. For a maximal allowed shear stress of 0.5 kPa [8], the maximal allowed fluid velocity is $v_{max} = 0.4\text{m s}^{-1} = O(1)\text{m s}^{-1}$.

- The maximum deformation in a simply supported beam is given by the formula

$$w_{max} = \left| \frac{5pL^4}{384EI} \right|. \tag{6}$$

E represents the Young's modulus of the material, in this case 20 kPa [1]. If we allow a maximal deformation of half the cylinder diameter, the maximal allowed fluid velocity is $v_{max} = O(1)\text{m s}^{-1}$.

3.3 Global scaffold behaviour

Finally, we assess the global behaviour of the scaffold. As shown in Figure (5) (top left) the global pressure difference over the scaffold is carried by the vertical columns that are formed by the struts. The material at the bottom of the scaffold should be able to withstand the compressive stresses resulting from this pressure difference. We

consider a single column, as indicated in Figure (5) (top right).
The maximum compressive stress at the bottom of this column is

$$\sigma_{max} = \left| \frac{F_{tot}}{A} \right|. \tag{7}$$

F_{tot} represents total force exerted on the bottom strut and is taken to be the accumulation of the drag forces exerted on the cylinders above: $F_{tot} = 0.07vLn$. The total number of layers is n (taken to be 10 for a 2 mm thick construct) and L is the length over which the drag force (that is carried by this particular column) works on the cylinders in each layer. The latter is equal to twice the diameter, as is indicated in Figure (5) (right). A is the cross section of the column. For a maximal allowed compressive stress of 2 kPa, the maximal allowed fluid velocity is: $v_{max} = 0.3\text{m s}^{-1} = O(1)\text{m s}^{-1}$. Note that it was assumed here that cylinders are slightly fused during the deposition process, while (Hertz-type) contact between cylinders can result in higher stress values.

As the above results consistently indicate high fluid flows are allowed without compromising the mechanical integrity of the the scaffold, a final check is performed by comparing the influence of the fluid flow on the scaffold to the effects of gravity. Comparing the gravitational acceleration (g) to the drag force per unit length divided by the mass per unit length ($F/\rho A$) indicated that the effects of fluid flow and gravity on the structure are equal for velocities $v_{max} = O(1)\text{cm s}^{-1}$. Only at velocities above this threshold do the effects of fluid flow surpass those of gravitation.

3.4 Conclusion

As the fluid velocities that are applied to the scaffold structure will be orders of magnitude below the m s^{-1} range, the mechanical integrity of the scaffold will not be jeopardised by the drag forces.

4 Growth of the extracellular matrix

4.1 Model

We consider a single spherical cell of radius a in an infinite, homogenous and isotropic medium. Over time, the cell produces matrix elements at a rate Q, which diffuse in the medium and bind with each other to form the extracellular matrix (ECM).

No distinction is made between collagen, proteoglycans or any other components of the ECM. The simplified model only distinguishes between mobile matrix components c_m and bound matrix components c_b. It is assumed that transport of mobile species can be described by a process of diffusion and binding, whereas the local concentration of bound matrix components depends only upon the binding rate and self-degradation.

The transport equations are then of the form

$$\frac{\partial}{\partial t}c_m - \frac{1}{r^2}\frac{\partial}{\partial r}\left(Dr^2\frac{\partial}{\partial r}c_m\right) = -k_B c_m, \tag{8a}$$

$$\frac{\partial}{\partial t}\, c_b = k_B c_m - k_D^0 c_b, \tag{8b}$$

with initial and boundary conditions

$$c_m = c_b = 0 \text{ at } t = 0, \tag{9a}$$

$$-D\frac{\partial}{\partial r}c_m = Q \quad \text{on} \quad r = a\ ,\ c_m \to 0 \quad \text{as} \quad r \to \infty. \tag{9b}$$

Here D is the diffusivity, k_B the binding rate, $k_D^0$the degradation constant and Q the rate at which the cell synthesises the matrix components.

In the simplest form of the model, D, Q and k_B are assumed to be constant. Although it appears to give significant insight on the dynamics of the system, this assumption has a limited range of validity, as will be discussed below.

We investigated more physical approaches by modelling D, Q and k_B as nonlinear functions of c_b and c_m, so that in general

$$k_B = k_B^0\, b\,(c_m, c_b)\,, \quad Q = Q_0\, q\,(c_m, c_b) \quad \text{and} \quad D = D_0\, d\,(c_m, c_b)\,, \tag{10}$$

where b, q and d are dimensionless (possibly nonlinear) functions of c_m or c_b.

We define the following dimensionless parameters:

$$\lambda = \frac{D_0}{k_B^0 a^2}\ , c_{ref} = \frac{Q_0 a}{D_0}\ , \quad k = \frac{k_D}{k_B^0}, \tag{11}$$

and write

$$r = a\tilde{r}, \quad c_b = c_{ref}\tilde{c}_b, \quad c_m = c_{ref}\tilde{c}_m, \quad t = \tilde{t}/k_B.$$

With physiological values of the parameters [14], $\lambda \approx 10$ and $k \approx 100$. With k_B^0 typically $1.2 \cdot 10^{-5}$ s^{-1} [4], one dimensionless time unit corresponds to approximately one day.

The evolution equations take the dimensionless form:

$$\frac{\partial}{\partial \tilde{t}}\tilde{c}_m - \frac{\lambda}{\tilde{r}^2}\frac{\partial}{\partial \tilde{r}}\left(d\left(c_m, c_b\right)\tilde{r}^2\frac{\partial}{\partial \tilde{r}}\tilde{c}_m\right) = -\tilde{c}_m\ b\left(c_m, c_b\right), \tag{12a}$$

$$\frac{\partial}{\partial \tilde{t}}\ \tilde{c}_b = \tilde{c}_m b\left(c_m, c_b\right) - k\tilde{c}_b, \tag{12b}$$

$$\tilde{c}_m = \tilde{c}_b = 0 \quad \text{at} \quad \tilde{t} = 0, \tag{12c}$$

$$\frac{\partial}{\partial \tilde{r}}\tilde{c}_m = -\frac{q\left(c_m, c_b\right)}{d\left(c_m, c_b\right)} \quad \text{on} \quad \tilde{r} = 1\ ,\ \tilde{c}_m \to 0 \quad \text{as} \quad \tilde{r} \to \infty. \tag{12d}$$

We first investigate the solution of (12) in the case where the functions b, q and d are constant and equal to unity. Then we compare with the solutions obtained for different forms of nonlinear functions.

4.2 Results

4.2.1 Constant coefficients

Here D, Q and k_B are assumed constant and equal to D_0, Q_0 and k_B^0 respectively.

Steady state In this case, it is straightforward to obtain the steady-state solution analytically:

$$\tilde{c}_m = \frac{\sqrt{\lambda}}{\sqrt{\lambda}+1}\frac{\exp\left(\frac{1-r}{\sqrt{\lambda}}\right)}{r}, \tag{13}$$

$$\tilde{c}_b = \frac{\sqrt{\lambda}}{\sqrt{\lambda}+1}\frac{\exp\left(\frac{1-r}{\sqrt{\lambda}}\right)}{kr}. \tag{14}$$

At steady state, the concentration of the ECM only differs with that of the mobile element by the ratio of timescales k between binding and degradation. The concentrations decay like $\exp\left(-r/\sqrt{\lambda}\right)/r$. The characteristic lengthscale for ECM growth around a single cell is then $\sqrt{\lambda}$. With physiological values of the parameters as given in [14], namely $\lambda = 10$, this implies that a population of cells within a gel can construct an interconnected network of ECM only if the cells' concentration is of order $30 \cdot 10^6$ cells·cm^{-3}.

Time-dependent solution An analytical solution for the time-dependent problem could be written in this particular case (constant coefficients). However, we concentrated our efforts on the numerical solution, since it could later be extended to address nonlinear models.

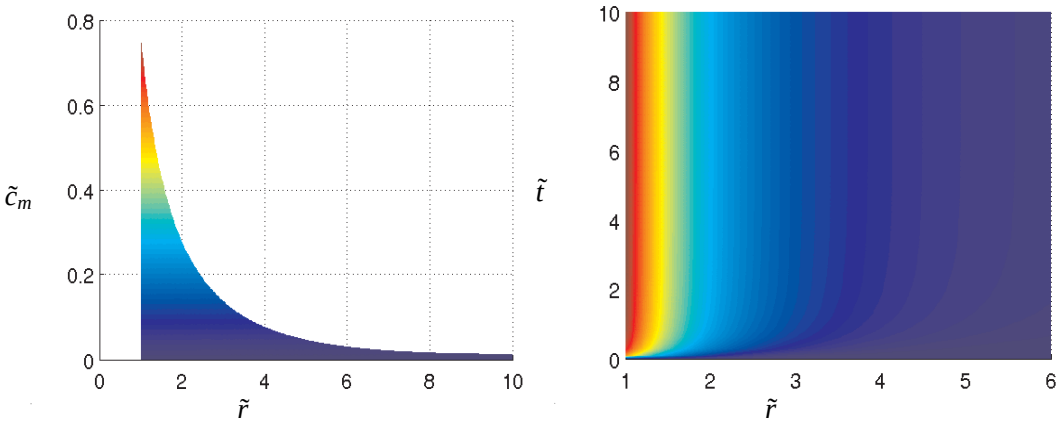

(a) Mobile species (b) Mobile species

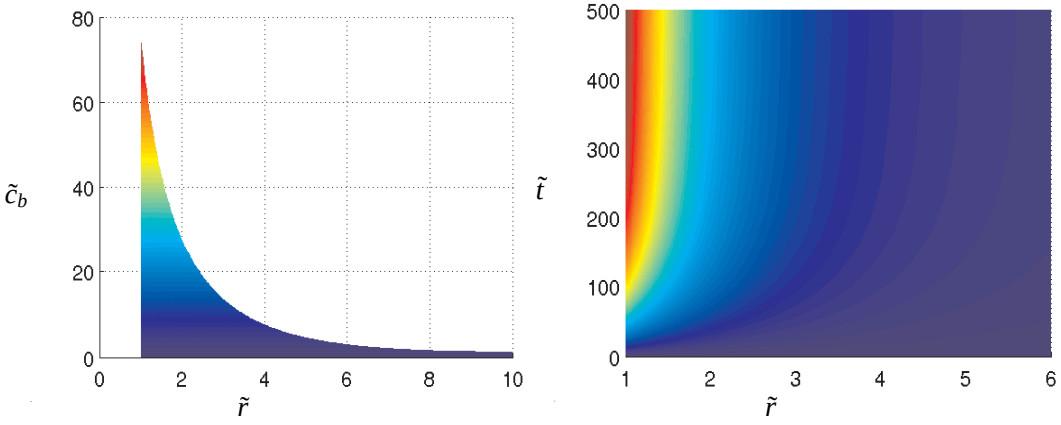

(c) ECM (d) ECM

Figure 8: Spatio-temporal evolution of the concentration of $\tilde{c}_b$ and $\tilde{c}_m$ with the model using constant parameters. Here $k = 100$. One dimensionless time unit is approximately one day, and the space unit is the cell radius.

4.2.2 Nonlinear models

Here D, Q and k_B are nonlinear functions of c_b and c_m, as described by (10).

It is physically sound to assume that the rate of binding between mobile elements should decrease once the ECM already built reaches a certain concentration. This is modelled by choosing for b a filter function with values close to 1 or close to 0 depending whether the ECM concentration c_b is smaller or larger than a certain threshold b_0. Physically, $c_b \approx b_0$ corresponds to the fully constructed (saturated) ECM. We choose for b a function of the form:

$$b\left(c_m, c_b\right) = 1 - \frac{c_b^\alpha}{b_0^\alpha + c_b^\alpha}, \tag{15}$$

with α an integer parameter.

Arguably, the rate at which the cell produces mobile elements should also depend on the amount of mobile elements already present in the medium close to the cell's membrane. We assume that the flux synthesised by the cell levels off when the concentration of mobile species c_m approaches a threshold q_0:

$$q\left(c_m, c_b\right) = 1 - \frac{c_m^2}{q_0^2 + c_m^2}. \tag{16}$$

The dimensionless values of the thresholds b_0 and q_0 are defined as $b_0 = c_{ref}\tilde{b}_0$ and $q_0 = c_{ref}\tilde{q}_0$.

Constant flux, nonlinear binding rate Figure (9) shows the evolution with space and time of the bound and mobile element densities in the case of a nonlinear binding rate (15) but a constant production rate of mobile elements from the cell ($q\left(c_m, c_b\right) = 1$).

Nonlinear flux, nonlinear binding rate Figure (10) shows distribution profiles in the case of non-constant production rate of mobile elements from the cell (15) and (16).

4.3 Comments

Quantitative measurements are scarce, but experiments suggest that ECM density near a cell does not decay exponentially with the distance from the cell surface (see Figure (11) for example). Our simplest model with constant coefficients therefore seems unphysical, although it seems to exhibit meaningful lengthscales for ECM synthesis (Figure (8)).

We then accounted for the fact that the rate of binding of mobile elements can be affected locally by the presence of already synthesised ECM (fewer binding sites are available). This was modelled by assuming that the rate of binding is close to k_B^0 when the concentration of ECM c_b is between 0 and a threshold value b_0, and decays to 0 when c_b is larger than b_0. The results (e.g. the density profiles) depend on the function chosen to model this smooth transition of the association rate from k_B^0 and 0. However, in all cases, the decay of c_b with r is no longer exponential (at least for $r = \mathcal{O}\left(1\right)$). In the

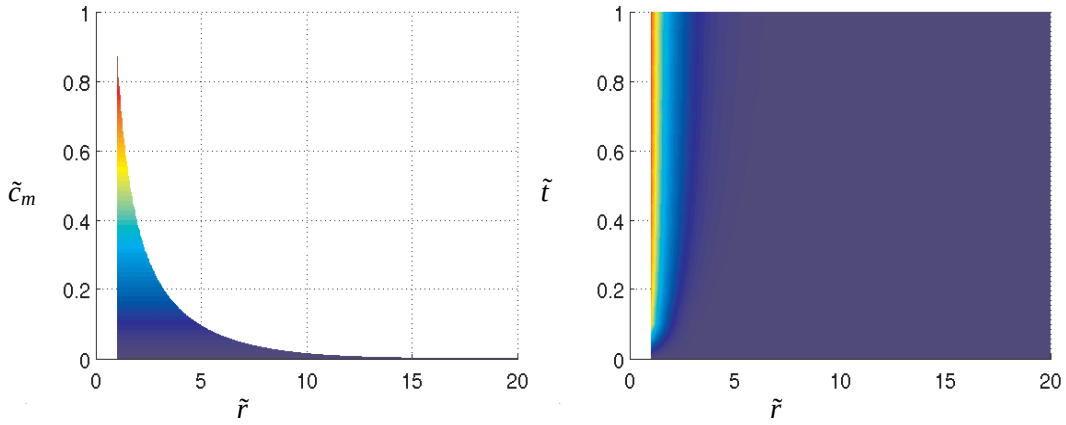

(a) Mobile species (b) Mobile species

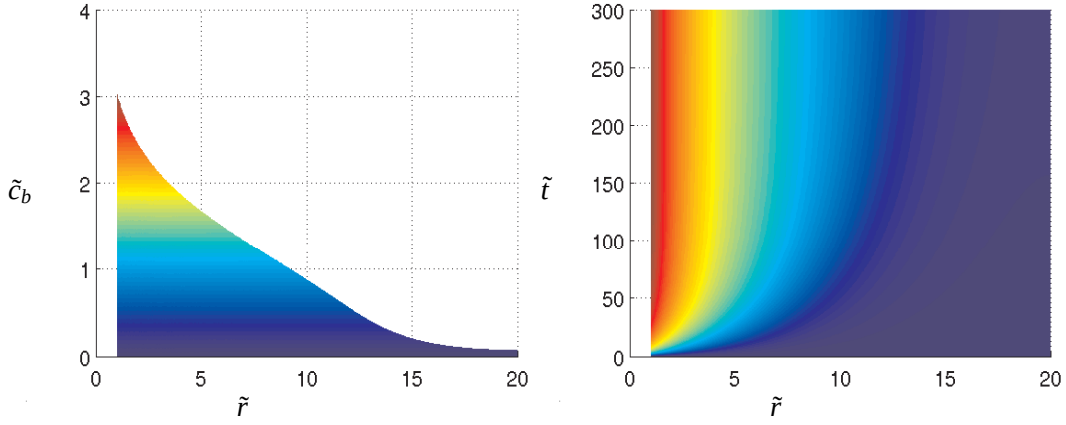

(c) ECM (d) ECM

Figure 9: Spatio-temporal evolution of the concentration of $\tilde{c}_b$ and $\tilde{c}_m$ with the model using the nonlinear function (15) for b and identity for q. Parameters used: $k = 100$, $\alpha = 3$ and $\tilde{b}_0 = 1$. One dimensionless time unit is approximately one day, and the space unit is the cell radius.

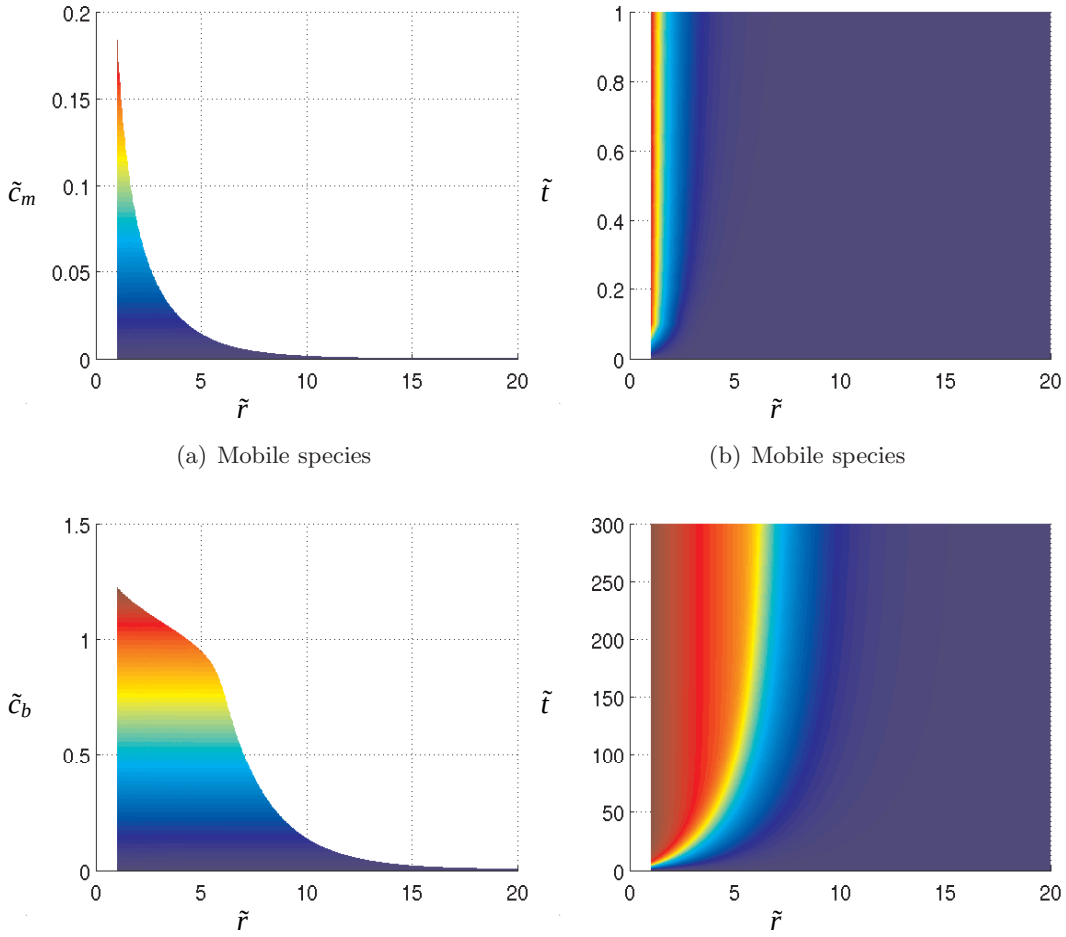

(a) Mobile species

(b) Mobile species

(c) ECM

(d) ECM

Figure 10: Spatio-temporal evolution of the concentration of $\tilde{c}_b$ and $\tilde{c}_m$ with the model using the nonlinear functions (15) and (16). Parameters used: $k = 100$, $\alpha = 13$, $\tilde{b}_0 = 1$ and $\tilde{d}_0 = 0.1$. One dimensionless time unit is approximately one day, and the space unit is the cell radius.

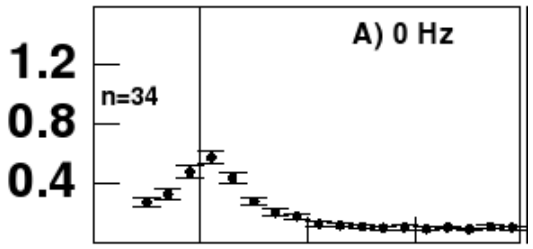

Figure 11: Grain density $\left(\mu\mathrm{m}^{-2}\right)$ in the vicinity of chondrocytes, showing incorporation of proteoglycans into the ECM. The vertical line delimits the cell surface. From [13].

example presented in figure 9 the decay is almost linear, qualitatively similar to some experimental data (Figure (11)).

Increasing the sharpness of the filter function $b\left(c_m, c_b\right)$ and adding a similar filter for the flux of mobile elements that the cell can produce leads to yet another family of distribution profiles. The concentration of ECM features a plateau in an annular region around the cell, then decays almost linearly.

Finally, we briefly examined the effect of having a non-constant diffusivity for the mobile elements. These results are not shown in the present report, but modelling diffusivity (10) with a nonlinear function of the concentrations c_m and c_b (as in (15)) tends to affect growth dynamics as well as the distribution profiles at steady states. This is not surprising physically since, in our model, diffusion is the only transport process.

5 Modelling the Transport Processes

We consider the scaffold to be comprised of separate gel and fluid systems. The gel is stationary and contains the cells that consume nutrients (mainly oxygen and glucose) and produce waste products (mainly lactate). The fluid is treated as an incompressible Newtonian (i.e. $\sim$ constant viscosity) fluid that flows due to a pressure gradient applied across the construct and carries the nutrients and waste products to/from the gel. These nutrients and waste products are therefore transported by advection and diffusion in the fluid region, but purely by diffusion in the gel region. We consider various different classes of scaffold structure in the analysis that follows. In each case we denote the fluid and gel regions by Ω_f and Ω_g respectively, and the boundary between the two by Γ. Subscripts f and g always distinguish between variables defined in Ω_f or Ω_g.

5.1 A Single Strand

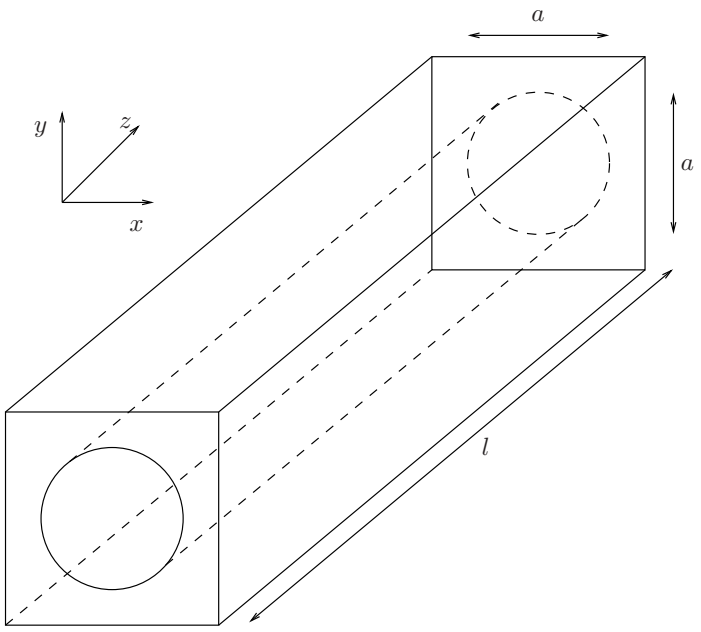

Figure 12: An example of a single strand setup

Firstly we consider a setup where the construct is made up of a single strand, as shown for example in Figure (12), to determine whether the multiple strand scaffold is necessary. The fluid is assumed to be a Newtonian fluid and is therefore described by

the Navier-Stokes equations

$$\nabla \cdot \mathbf{u} = 0 \text{ in } \Omega_f, \tag{17}$$

$$\rho \left(\frac{\partial \mathbf{u}}{\partial t} + (\mathbf{u} \cdot \nabla \mathbf{u}) \right) = -\nabla p + \mu \nabla^2 \mathbf{u} \text{ in } \Omega_f, \tag{18}$$

$$\mathbf{u} = 0 \text{ on } \Gamma, \tag{19}$$

where $\mathbf{u} = (u, v, w)$ denotes the fluid velocity, p the fluid pressure, ρ the fluid density and μ the fluid viscosity. The no slip boundary condition (19) is imposed on the fluid-gel interface as there is no fluid flow in the gel. The oxygen transport problem is described by

$$\frac{\partial c_f}{\partial t} + \mathbf{u} \cdot \nabla c_f = D_f \nabla^2 c_f \text{ in } \Omega_f, \tag{20}$$

$$\frac{\partial c_g}{\partial t} = D_g \nabla^2 c_g - k_o \phi c_g \text{ in } \Omega_g, \tag{21}$$

$$c_f = c_g \text{ on } \Gamma, \tag{22}$$

$$D_f \frac{\partial c_f}{\partial n} = D_g \frac{\partial c_g}{\partial n} \text{ on } \Gamma, \tag{23}$$

where c corresponds to the oxygen concentration. Equation (20) describes the transport of oxygen by advection (with the fluid velocity $\mathbf{u}$) and diffusion (with diffusion coefficient D_f) in the fluid. In the gel, oxygen diffuses (with diffusion coefficient D_g) and is consumed by the cells (with consumption coefficient $k_1\phi$ where ϕ is the cell density), as shown by equation (21). We have assumed a linear consumption rate as an approximation to Michaelis-Menten kinetics (valid for the concentration range here). The boundary conditions on the fluid-gel interface as given by equations (22) and (23), which correspond to continuity of concentration and flux on Γ. Similarly the lactate transport problem is described by

$$\frac{\partial l_f}{\partial t} + \mathbf{u} \cdot \nabla l_f = \mathcal{D}_f \nabla^2 l_f \text{ in } \Omega_f, \tag{24}$$

$$\frac{\partial l_g}{\partial t} = \mathcal{D}_g \nabla^2 l_g + k_l \phi l_g \text{ in } \Omega_g, \tag{25}$$

$$l_f = l_g \text{ on } \Gamma, \tag{26}$$

$$\mathcal{D}_f \frac{\partial l_f}{\partial n} = \mathcal{D}_g \frac{\partial l_g}{\partial n} \text{ on } \Gamma, \tag{27}$$

where l corresponds to the lactate concentration. Clearly lactate behaves in the same manner as oxygen, but with diffusion coefficients $\mathcal{D}_f$ and $\mathcal{D}_g$ and a linear production rate term $+k_2\phi l_g$ in the gel. Table (1) gives realistic parameter values.

[1] diffusion coefficients for lactate are unclear and some estimates are of the same order of magnitude as the oxygen diffusion coefficients

[2] $k_1 = 10^{-16}$ m^3 s^{-1} cell^{-1} corresponds to the anaerobic extreme

[3] range of values for k_2 are based on the lactate production rate being 2× glucose consumption rate - 1/3× oxygen consumption rate, without the medium being buffered, and so represent a "worst case" scenario

Parameter	Value	Unit	Description
a	2×10^{-4}	m	typical strand diameter
l	5×10^{-3}	m	typical strand length
ρ	10^3	kg m^{-3}	fluid density
μ	10^{-3}	kg m^{-1} s^{-1}	fluid viscosity
D_f	3×10^{-9}	m^{2}s^{-1}	oxygen diffusion coefficient in fluid
D_g	2.6×10^{-9}	m^{2}s^{-1}	oxygen diffusion coefficient in gel
$\mathcal{D}_f$	4×10^{-11}	m^{2}s^{-1}	lactate diffusion coefficient in fluid[1]
$\mathcal{D}_g$	3.2×10^{-11}	m^{2}s^{-1}	lactate diffusion coefficient in gel
ϕ	$8 \times 10^{12} - 25 \times 10^{12}$	cells m^{-3}	cell density in gel
k_1	$10^{-18} - 10^{-16}$	m^3 s^{-1} cell^{-1}	oxygen consumption rate[2]
k_2	$10^{-17} - 10^{-16}$	m^3 s^{-1} cell^{-1}	lactate production rate[3]

Table 1: Table of typical parameter values (from [10], [2] or personal communication).

We now scale all variables to determine which of the processes (advection, diffusion or consumption/production) dominates both radially through the gel and also down the gel length (in the z-direction). There is not clear data on the typical fluid velocities (a pressure gradient is applied across the construct to generate the fluid flow; however, this gradient is unknown) therefore we scale the fluid velocity $\mathbf{u}$ with an unknown U and derive bounds on U that differentiate between physical situations. For a general length scale d,

$$\text{advective timescale} = \frac{d}{U}, \tag{28}$$

$$\text{diffusive timescale} = \frac{d^2}{D}, \tag{29}$$

$$\text{consumption/production timescale} = \frac{1}{k\phi}, \tag{30}$$

(for example the advective timescale is derived by balancing the terms on the lefthand side of (20) or (24)). When $d = a$ this corresponds to the transport timescale radially across the gel strand, and when $d = l$ to that down the gel strand in the z-direction. A

summary of the relevant timescales in each direction is given in Table (5.1). It is clear that, for these parameter values, diffusion of oxygen will dominate over consumption in the gel (13s $\ll$ 400s) and so the growth of the cells in the gel will not be impeded by a lack of oxygen. On this basis, there is no necessity for multiple strands in the construct. This will always be the case unless the diffusive and consumption timescales in the gel are of the same size (as then the growth of the cells will be diffusion limited) and this will occur when the strand diameter a increases to a critical value. The diffusive and consumption timescales balance when $a = a_{max}$ and

$$\frac{a_{max}^2}{D_g} = \frac{1}{k_1\phi}. \tag{31}$$

This formula could be used to determine typical values for the maximum strand diameter a as a function of the cell density ϕ. For example, assuming $k_1 = 10^{-18}$,

$$a_{max} = \sqrt{\frac{D_g}{k_1\phi}} = \frac{50990}{\sqrt{\phi}} \tag{32}$$

is the maximum strand diameter. Similarly

$$a_{max} = \frac{\sqrt{2.6 \times 10^{-9}}}{k_1\phi} \tag{33}$$

can be considered as a function of the consumption term $k_1\phi$. Plots of both of these cases are shown in Figure (13).

Description	Formula	Timescale (secs)
Advection in z-direction	$\frac{l}{U}$	$\frac{5}{U} \times 10^{-3}$
Oxygen diffusion down strand in gel	$\frac{l^2}{D_g}$	9.6×10^3
Oxygen diffusion radially in gel	$\frac{a^2}{D_g}$	15
Oxygen diffusion in z-direction in fluid	$\frac{l^2}{D_f}$	8.3×10^3
Oxygen diffusion radially in fluid	$\frac{a^2}{D_f}$	13
Oxygen consumption in gel	$\frac{1}{k_1\phi}$	$4 \times 10^2 - 1.25 \times 10^5$
Lactate diffusion down strand in gel	$\frac{l^2}{\mathcal{D}_g}$	7.8×10^5
Lactate diffusion radially in gel	$\frac{a^2}{\mathcal{D}_g}$	1250
Lactate diffusion in z-direction in fluid	$\frac{l^2}{\mathcal{D}_f}$	6.25×10^5
Lactate diffusion radially in fluid	$\frac{a^2}{\mathcal{D}_f}$	1000
Lactate production in gel	$\frac{1}{k_2\phi}$	$4 \times 10^2 - 1.25 \times 10^4$

Table 2: Transport timescales

However, the transport timescales for lactate differ significantly because the diffusion coefficients for lactate $\mathcal{D}_f$ and $\mathcal{D}_g$ are approximately 100 times smaller than those for oxygen. Lactate is produced in the strand as a waste production of respiration, and will be toxic to the cells above a critical concentration $l^* = 10\text{mol m}^{-3}$ [2]. It is therefore crucial that the lactate is eliminated from the construct before this critical concentration l^* is reached. Once the lactate is produced in the gel, it can only be transported into the fluid region by diffusion. It is therefore necessary for the timescale for lactate diffusion radially in the gel to balance the timescale for lactate production. This gives an order of magnitude for the strand diameter a determined from

$$\frac{a^2}{\mathcal{D}_g} = \frac{1}{k_2\phi} \;\Rightarrow\; a = \sqrt{\frac{\mathcal{D}_g}{k_2\phi}}. \tag{34}$$

For example, assuming $k_2 = 10^{-17}$,

$$a = \frac{1789}{\sqrt{\phi}} \tag{35}$$

gives the strand diameter as a function of the cell density. Similarly

$$a = \sqrt{\frac{3.2 \times 10^{-11}}{k_2\phi}} \tag{36}$$

gives a as a function of $k_2\phi$. Plots of both of these cases are shown in Figure (13). The maximum values of a required are now approximately 100 times smaller than those required to prevent cell oxygen deprivation. This supports the use of a construct made up of multiple strands of gel as opposed to a single strand in order to introduce sufficient cells to the construct whilst limiting their lactate exposure.

Once the lactate has diffused into the fluid region, it must be removed from the construct to prevent it diffusing back into the gel and potentially causing cell death. In the fluid, advection dominates over lactate diffusion and so by balancing the advective and lactate production timescales we find an approximation for the minimum fluid velocity required to remove the lactate. This balancing gives

$$\frac{l}{U} = \frac{1}{k_2\phi}. \tag{37}$$

Based on the result above, we choose a maximum value of a at a given cell density as it is easier to print strands with a larger diameter. For example, consider the case when

$$\phi = 1.7 \times 10^4 \text{ cells mm}^{-3}\ ,\ k_2\phi = 1.4 \times 10^{-4}\ \text{s}^{-1}\ ,\ a = 435\ \mu\text{m}. \tag{38}$$

Then,

$$U = lk_2\phi = 5 \times 10^{-3} \times 1.4 \times 10^{-4} = 7 \times 10^{-7}\text{m s}^{-1}. \tag{39}$$

is the minimum velocity required to remove lactate from the construct.

5.1.1 Conclusions

Due to the small diffusion coefficients of lactate in both gel and fluid, it is necessary to introduce a construct that is made up of multiple strands. We therefore reject the single strand setup, and use homogenization theory to determine the flow and transport properties for a construct with a multiple strand scaffold.

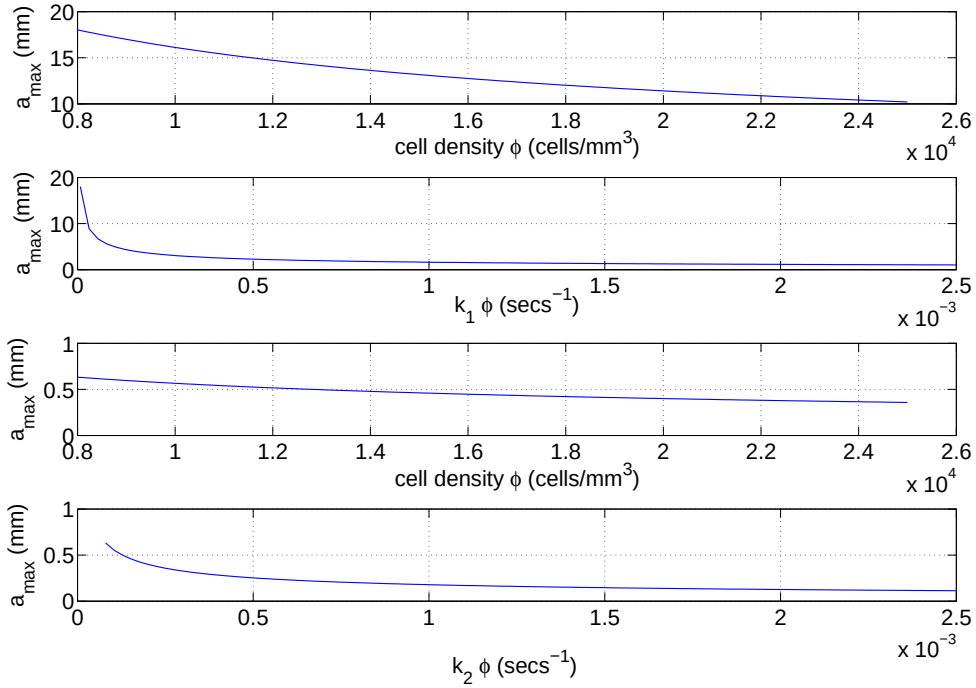

Figure 13: *Top two graphs* : Plots of the maximum strand diameter for varying cell density ϕ and consumption term $k_1\phi$. These represent the case when cell growth will be limited by the diffusion of oxygen. *Bottom two graphs* : plots of the strand diameter for varying cell density ϕ and production term $k_2\phi$. These represent the maximum strand diameter required to remove lactate from the gel

5.2 Homogenization Approach

Homogenization is a mathematical "averaging" technique. It is applicable to systems with well-separated length scales and aims to find the "average" properties of a whole structure based on its detailed substructure. The construct in this situation is comprised of a scaffold of fine gel strands and surrounding fluid. The strand separation d is much smaller than the construct dimensions, so that if we define a dimensionless parameter by

$$\varepsilon = \frac{d}{l}, \tag{40}$$

then $\varepsilon \ll 1$. We consider the two different scales characterized by these two length scales d and l. "Zooming" into a particular point in the construct reveals the strand structure in detail and we refer to this "zooming level" as the *local scale* or *microscale*. In contrast "zooming" out allows us to consider the construct as a whole and we refer to this "zooming level" as the *global scale* or *macroscale*. The objective of homogenisation is to start from the known flow and transport properties on the local scale and use a mathematical technique (called multiple scales) to move from the local to the global descriptions and so derive the flow and transport equations on the global scale. The key assumption necessary to perform homogenization is that the local structure is periodic. This means that the construct is in fact made up of a single building block that repeats itself like a jigsaw puzzle to form the construct. Fortunately this is a realistic assumption here because the scaffold is formed so regularly (refer to Figure (1)). Here we assume that the strands have a constant cell density, although in future it would be feasible to build in a cell density that varies on the global scale as would be more realistic for tissue engineering. An important advantage of the homogenisation process is that it can be completed without having to prescribe the exact local structure and so it is possible to investigate many different forms of scaffold easily. Also, the permeability tensor for the structure is derived automatically as a direct result of completing the fluid homogenization problem. Figure (14) shows the local and global scales for an example local periodic geometry. Figure (15) shows how this local geometry repeats itself to form the strand-fluid structure.

We consider the fluid and oxygen processes turn.

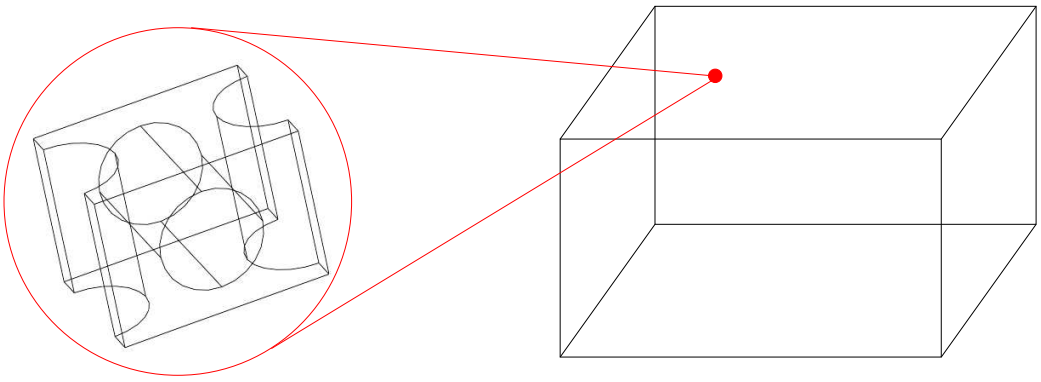

Figure 14: The homogenization approach.

5.2.1 Fluid Problem

We consider a periodic cell with dimension d, for example that shown in Figure (14). We denote the total volume by V and this is comprised of the fluid volume V_f and gel volume V_g such that $V = V_f \cup V_g$. We denote the interface between the fluid and gel regions by $\Sigma = 0$. As previously explained, we model the fluid as a Newtonian fluid described by the Navier-Stokes equations (17)-(18) in V_f subject to the no-slip boundary condition (19) on the interface $\Sigma = 0$. Before embarking on the mathematical analysis of the model, we perform a procedure called *nondimensionalisation*. Nondimensionalisation is a technique used to determine the dominant terms in a system by rescaling all variables with typical values (and so also removes units from the system). We nondimensionalise equations (17)-(19) with the scalings

$$\mathbf{x} = d\mathbf{x}' \ , \ \mathbf{u} = U\mathbf{u}' \ , \ p = Pp' + p_0, \ t = \frac{l}{U}t', \tag{41}$$

and define nondimensional parameters by

$$\varepsilon = \frac{d}{l} \ , \ \mathrm{Re} = \frac{\rho U d}{\mu}. \tag{42}$$

Here d is the typical dimension of the periodic cell. U is the typical velocity scale and is not known by the experimentalists, although our previous calculation (39) suggests that $U = \mathcal{O}\left(10^{-7}\right)$ is a reasonable estimate. P is a typical pressure scale, and p_0 is the ambient pressure. We have nondimensionalised t with l/U - the global advective timescale. This is because based on the results of the previous section (see Table (5.1)), when $U = \mathcal{O}\left(10^{-7}\right)$ advection and diffusion balance on the global scale. The nondimensional parameters (42) have no units and represent the ratio of various physical effects. Therefore the size of these parameters determines which physical effects dominate. Scientifically, ε represents the ratio of the two different length scales d and l, and

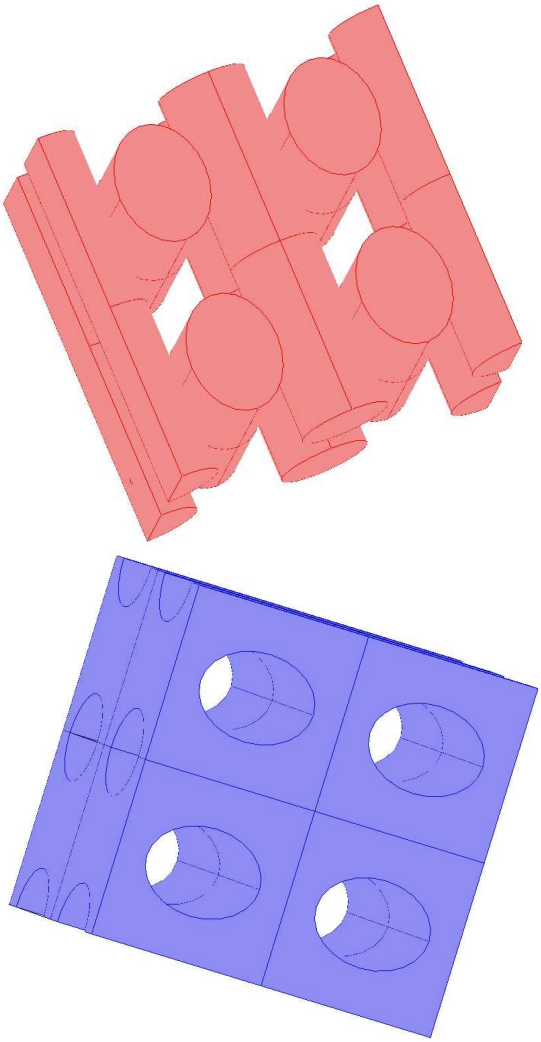

Figure 15: An example of a periodic local structure. The red regions are the gel strands and the blue regions the fluid.

the Reynolds number Re represents the ratio of inertial to viscous forces in the fluid. Using the parameter values in Table (1) (with $d = 2a$), we estimate

$$\varepsilon = 0.08, \tag{43}$$

$$\mathrm{Re} = 4 \times 10^{-5} = \mathcal{O}\left(\varepsilon^4\right). \tag{44}$$

Clearly the Reynolds number Re is very small which indicates that viscous forces dominate over inertial forces in the fluid. This type of flow is called *Stokes flow* and we choose the pressure scale to be $P = \frac{\mu U l}{d^2}$ as is typical for this type of flow in this regime.

Dropping the primes, the system then becomes

$$\boldsymbol{\nabla} \cdot \mathbf{u} = 0 \text{ in } V_f, \tag{45}$$

$$\varepsilon \mathrm{Re} \left(\varepsilon \frac{\partial \mathbf{u}}{\partial t} + (\mathbf{u} \cdot \boldsymbol{\nabla}) \mathbf{u} \right) = -\boldsymbol{\nabla} p + \epsilon \nabla^2 \mathbf{u} \text{ in } V_f, \tag{46}$$

$$\mathbf{u} = \mathbf{0} \text{ on } \Sigma = 0. \tag{47}$$

We now use an analytical technique called *multiple scales* to investigate the behaviour this system on both the local and global length scales simultaneously. As $\varepsilon \ll 1$, the local and global length scales are well-separated so we define $\mathbf{X}$ and $\mathbf{x}$ to be the local and global length scales respectively. $\mathbf{X}$ and $\mathbf{x}$ are related to each other through

$$\mathbf{x} = \varepsilon \mathbf{X}. \tag{48}$$

Under the assumption of scale separation we treat $\mathbf{x}$ and $\mathbf{X}$ as independend variables and expand the gradient and laplacian operators through

$$\boldsymbol{\nabla} = \boldsymbol{\nabla}_X + \varepsilon \boldsymbol{\nabla}_x \ , \ \nabla^2 = \nabla_X^2 + 2\varepsilon \boldsymbol{\nabla}_X \cdot \boldsymbol{\nabla}_x + \epsilon^2 \nabla_x^2. \tag{49}$$

Justifying the validity of this assumption in the limit as $\varepsilon \to 0$ is one of the main issues in rigorous homogenization theory and is treated in [12], among other texts. We now denote the fluid-gel boundary by $\Sigma_\varepsilon = 0$. The rescaled equations in V_f become

$$\boldsymbol{\nabla}_X \cdot \mathbf{u} + \epsilon \boldsymbol{\nabla}_x \cdot \mathbf{u} = 0, \tag{50}$$

$$\begin{aligned} \varepsilon \mathrm{Re} \left(\varepsilon \frac{\partial \mathbf{u}}{\partial t} + (\mathbf{u} \cdot \boldsymbol{\nabla}_X) \mathbf{u} + \varepsilon (\mathbf{u} \cdot \boldsymbol{\nabla}_x) \mathbf{u} \right) = & - \boldsymbol{\nabla}_X p - \varepsilon \boldsymbol{\nabla}_x p + \varepsilon \nabla_X^2 \mathbf{u} \\ & + 2\varepsilon^2 \boldsymbol{\nabla}_x \cdot \boldsymbol{\nabla}_X \mathbf{u} + \varepsilon^3 \nabla_x^2 \mathbf{u}. \end{aligned} \tag{51}$$

The boundary condition remains

$$\mathbf{u} = \mathbf{0} \text{ on } \Sigma_\varepsilon = 0. \tag{52}$$

We perform multiple scales expansions

$$\mathbf{u} = \mathbf{u}^{(0)}(\mathbf{x}, \mathbf{X}) + \varepsilon \mathbf{u}^{(1)}(\mathbf{x}, \mathbf{X}) + \dots \tag{53}$$

$$p = p^{(0)}(\mathbf{x}, \mathbf{X}) + \varepsilon p^{(1)}(\mathbf{x}, \mathbf{X}) + \dots \tag{54}$$

where the $\mathbf{u}^{(j)}$ and $p^{(j)}$ are assumed to be periodic in $\mathbf{X}$. Equating powers of ε (to avoid singularity in the limit as $\varepsilon \to 0$) in equation (50),

$$\boldsymbol{\nabla}_X \cdot \mathbf{u}^{(0)} = 0, \tag{55}$$

$$\boldsymbol{\nabla}_X \cdot \mathbf{u}^{(1)} + \boldsymbol{\nabla}_x \cdot \mathbf{u}^{(0)} = 0, \tag{56}$$

and in equation (51),

$$\boldsymbol{\nabla}_X p^{(0)} = 0 \ \Rightarrow p^{(0)} = p^{(0)}(\mathbf{x}), \tag{57}$$

$$\boldsymbol{\nabla}_X p^{(1)} - \nabla_X^2 \mathbf{u}^{(0)} = -\boldsymbol{\nabla}_x p^{(0)}. \tag{58}$$

Finally the boundary condition (52) gives

$$\mathbf{u}^{(m)} = 0 \text{ on } \Sigma_\varepsilon(\mathbf{X}) = 0, \text{ for } m = 0, 1, \dots . \tag{59}$$

Firstly note that from (57), $p^{(0)}$ is a function of the global variable $\mathbf{x}$ only and so is constant on the local scale. Hence, $p^{(1)}$ can be thought of as the local adjustment to $p^{(0)}$. Equations (55)-(59) define a sequence of boundary-value problems in the periodic cell. We exploit linearity and let

$$\mathbf{u}^{(0)} = -\frac{\partial p^{(0)}}{\partial x_j}\mathbf{w}^j, \tag{60}$$

$$p^{(1)} = -P_j\frac{\partial p^{(0)}}{\partial x_j} + \overline{p}^{(1)}, \tag{61}$$

where $\mathbf{w}^j(\mathbf{X}, \mathbf{x})$, $P_j(\mathbf{X}, \mathbf{x})$ are to be determined. The term $\overline{p}^{(1)}(\mathbf{x})$ is included here for completeness, but does not need to be determined unless we want to find the $\mathcal{O}(\varepsilon)$ correction $\mathbf{u}^{(1)}$ to the velocity profile. The cell problem is then given by

$$\boldsymbol{\nabla}_X \cdot \mathbf{w}^j = 0, \tag{62}$$

$$\boldsymbol{\nabla}_X P_j = \nabla_X^2 \mathbf{w}^j + \mathbf{e}_j, \tag{63}$$

$$\mathbf{w}^j = 0 \text{ on } \Sigma_\varepsilon(\mathbf{X}) = 0, \tag{64}$$

where $\mathbf{w}^j$ and P_j are periodic in $\mathbf{X}$. This canonical cell problem (62)-(64) could be solved numerically (or possibly analytically) for a prescribed local configuration. Once solved, we take averages over the fluid domain with respect to $\mathbf{X}$, defined by

$$\langle g \rangle = \frac{1}{|V|}\iiint_{V_f} g \mathrm{d}V, \tag{65}$$

where $|V|$ is the total volume of the periodic cell, and V_f is the fluid volume in the cell. Defining

$$K_{ij} = \frac{1}{|V|}\iiint_{V_f} w_i^j \mathrm{d}V, \tag{66}$$

we then take averages of (60). Integrating (60) over the fluid domain V_f and noting that $p^{(0)}$ is a function of the global variable $\mathbf{x}$ only (so can be brought out of the integral) gives Darcy's Law

$$\langle \mathbf{u}^{(0)} \rangle = -\mathbf{K} \cdot \boldsymbol{\nabla}_x p^{(0)}. \tag{67}$$

Therefore $\mathbf{K}$ is the permeability tensor for the construct, given by (66). Finally, consider (56), and integrate over the fluid domain to give

$$\iiint_{V_f} \boldsymbol{\nabla}_X \cdot \mathbf{u}^{(1)} \mathrm{d}V = -\boldsymbol{\nabla}_x \cdot \left(\iiint_{V_f} \mathbf{u}^{(0)} \mathrm{d}V \right). \tag{68}$$

However, using the Divergence Theorem, boundary condntion (59) with $m = 1$ and the periodicity of $\mathbf{u}^{(1)}$ on the cell,

$$\iiint_{V_f} \boldsymbol{\nabla}_X \cdot \mathbf{u}^{(1)} \mathrm{d}V = \iint_{\partial V_f} \mathbf{u}^{(1)} \cdot \mathbf{n} \mathrm{d}S = 0. \tag{69}$$

Hence,

$$\boldsymbol{\nabla}_x \cdot \langle \mathbf{u}^{(0)} \rangle = 0. \tag{70}$$

This can be solved with the Darcy equation (67) to determine the fluid pressure and velocity in the construct.

5.2.2 Numerical Results : Fluid

We used a finite elements package *COMSOL Multiphysics* to solve the cell problem (62)-(64) above on the domain in Figure (15). Figures (16)-(18) show the results for $j = 1, 2, 3$. In particular, *COMSOL Multiphysics* can also be used to calculate the components of the nondimensional permeability tensor (66). This gives

$$\mathbf{K} = \begin{pmatrix} \alpha & 0 & 0 \\ 0 & \alpha & 0 \\ 0 & 0 & \beta \end{pmatrix} \tag{71}$$

where $\alpha = 0.044$, $\beta = 0.062$. Redimensionalising then gives the tensor

$$\mathbf{M} = (n + a)^2 \mathbf{K}, \tag{72}$$

where n is the strand diameter and a is the strand separation. We ran out of time to investigate other local structures, but this could be done easily in future and the corresponding permeability tensors could be calculated using *COMSOL Multiphysics*.

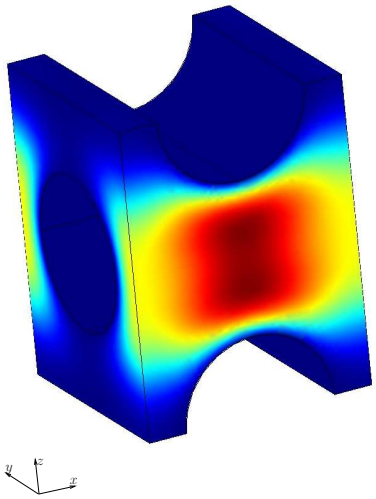

Figure 16: The solution $\mathbf{w}^{(1)}$ of the cell problem (62)-(64) when $j = 1$ so the forcing is in the X direction. Represents the leading-order local variation in the velocity profile.

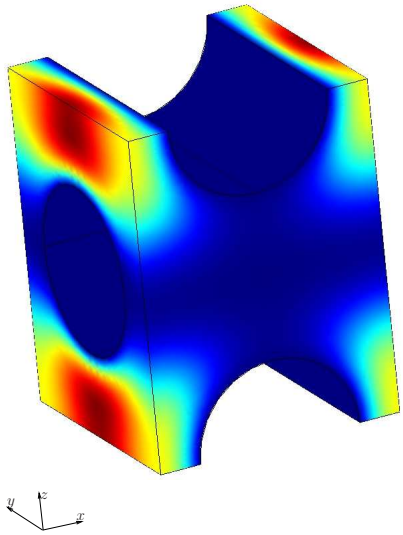

Figure 17: The solution $\mathbf{w}^{(2)}$ of the cell problem (62)-(64) when $j = 2$ so the forcing is in the Y direction. Represents the leading-order local variation in the velocity profile.

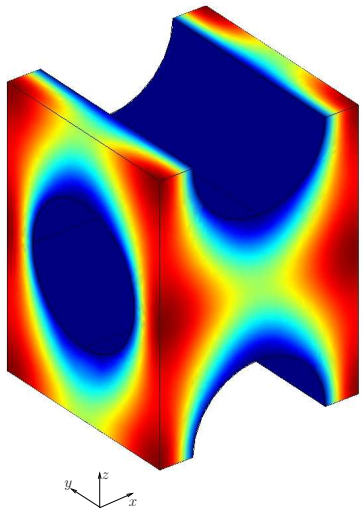

Figure 18: The solution $\mathbf{w}^{(3)}$ of the cell problem (62)-(64) when $j = 3$ so the forcing is in the Z direction. Represents the leading-order local variation in the velocity profile.

5.2.3 Oxygen Problem

We now consider the oxygen transport problem using the homogenization technique. The dimensional equations describing the oxygen transport on the local scale in the periodic cell are given by

$$\frac{\partial c_f}{\partial t} + \boldsymbol{\nabla} \cdot (c_f \mathbf{u} - D_f \boldsymbol{\nabla} c_f) = 0 \text{ in } V_f, \tag{73}$$

$$\frac{\partial c_g}{\partial t} - \boldsymbol{\nabla} \cdot (D_g \boldsymbol{\nabla} c_g) = -k_1 \phi c_g \text{ in } V_g, \tag{74}$$

where both equations have been written in conservation form. On the fluid-gel interface we must impose two boundary conditions and we choose continuity of the oxygen concentration and continuity of the oxygen flux,

$$c_f = c_g \text{ on } \Sigma = 0, \tag{75}$$

$$D_f \boldsymbol{\nabla} c_f \cdot \mathbf{n} = D_g \boldsymbol{\nabla} c_g \cdot \mathbf{n} \text{ on } \Sigma = 0. \tag{76}$$

(Note that as $\mathbf{u} = 0$ on $\Sigma = 0$, only the diffusive fluxes and not the advective flux in V_f contribute to the flux continuity condition (76)). We nondimensionalise as for the fluid case using the scalings (41) and

$$c = Cc' \ , \ D = D_f D', \tag{77}$$

and define additional dimensionless parameters

$$\mathrm{Pe}_l = \frac{Ud}{D_f} \ , \ \mathrm{Da}_l = \frac{k_1 d^2 \phi}{D_f}. \tag{78}$$

We also let $D_g = D_f D_g'$, but then drop the ' (so that from now onwards D_g is dimensionless and refers to the ratio of diffusion coefficients). The local Péclet number Pe_l represents the ratio of diffusive to advective timescales on the local lengthscale d. The local Damköhler number Da_l represents the ratio of diffusive to consumptive timescales, again on the local lengthscale d. (Note that therefore if $\mathrm{Pe} < 1$ then diffusion dominates over advection as advection will occur on a longer timescale, etc). Using the parameter values in Table (1) with the velocity scale $U = 7 \times 10^{-7}\mathrm{m\ s}^{-1}$ we estimate

$$\mathrm{Pe}_l = 0.09 = \mathcal{O}(\varepsilon). \tag{79}$$

Therefore the diffusion dominates over advection on the local lengthscale. We let

$$\mathrm{Pe}_l = \varepsilon \overline{\mathrm{Pe}_l} \tag{80}$$

where $\overline{\mathrm{Pe}_l}$ is the reduced local Péclet number and is $\mathcal{O}(1)$. The global Péclet number, defined as the ratio of diffusive to advective timescales on the global lengthscale and given by

$$\mathrm{Pe}_g = \frac{Ul}{D_f}, \tag{81}$$

is therefore $\mathcal{O}(1)$ as expected from Table (5.1) as advection and diffusion balance each other on the global scale. In contrast the size of the local Damköhler number Da_l depends on the consumption rate k_1 and cell density ϕ in the gel, which can take a range of values. The global Damköhler number Da_g represents the ratio of diffusive to consumptive timescales on the global lengthscale l and is given by

$$\mathrm{Da}_g = \frac{k_1 l^2 \phi}{D_f}. \tag{82}$$

The local and global Damköhler numbers are therefore related through

$$\mathrm{Da}_l = \varepsilon^2 \mathrm{Da}_g. \tag{83}$$

Given that oxygen is supplied to the gel by advection and diffusion (which both occur on the same timescale on the global scale), Da_g must be at most $\mathcal{O}(1)$ (otherwise consumption occurs faster than diffusion/advection which is impossible unless we factor in a timescale for growth). Therefore Da_l must be at most $\mathcal{O}\left(\varepsilon^2\right)$. This gives a maximum bound for the product $k_1\phi$ given by

$$(k_1\phi)_{max} = \frac{\mathrm{Da}_l D_f}{d^2} = \frac{\varepsilon^2 D_f}{d^2} = 1.2 \times 10^{-4}\ \mathrm{s}^{-1}. \tag{84}$$

The range of values provided by the experimentalists meant that $k_1\phi$ could be as large as $2.5 \times 10^{-3}\ \mathrm{s}^{-1}$, so (84) effectively imposes a maximum on the cell density ϕ, given a chosen oxygen consumption rate. For example, Figure (19) shows how the maximum cell density ϕ_{max} varies when the consumption rate k_1 varies from $10^{-18} - 10^{-16}\ \mathrm{m}^3\ \mathrm{s}^{-1}$ cell^{-1}.

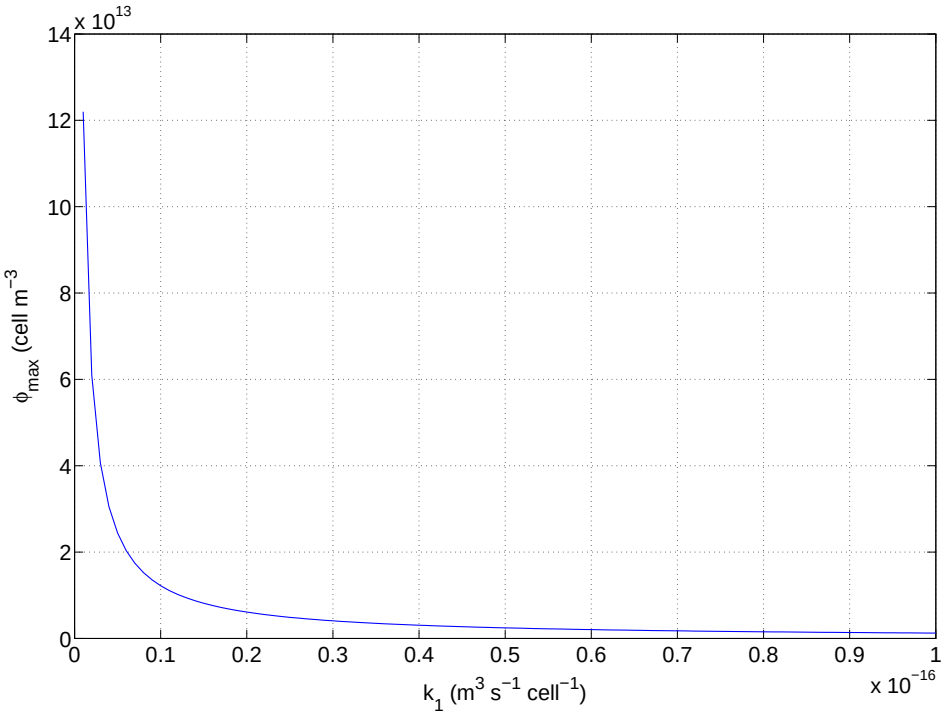

Figure 19: A graph showing how the maximum cell density ϕ_{max} varies with the oxygen consumption rate k_1.

$k_1\phi$	Da_l
1.2×10^{-4}	$\mathcal{O}\left(\epsilon^2\right)$
1×10^{-5}	$\mathcal{O}\left(\epsilon^3\right)$

Table 3: Table comparing $k_1\phi$ with the local Damköhler number Da_l.

Table (3) shows how the order of magnitude of Da_l varies with the product $k_1\phi$, and we consider the two cases when $\mathrm{Da}_l = \mathcal{O}\left(\varepsilon^2\right)$ and when $\mathrm{Da}_l = \mathcal{O}\left(\varepsilon^3\right)$ in turn as they give different results for the homogenized transport equation. Using the fact that $\boldsymbol{\nabla} \cdot \mathbf{u} = 0$ and dropping the primes, the nondimensionalised system can now be written

as

$$\varepsilon\overline{\mathrm{Pe}}\left(\varepsilon\frac{\partial c_f}{\partial t}+\mathbf{u}\cdot\boldsymbol{\nabla}c_f\right)=\nabla^2 c_f \text{ in } V_f, \tag{85}$$

$$\varepsilon^2\overline{\mathrm{Pe}}\frac{\partial c_g}{\partial t}=D_g\nabla^2 c_g-\mathrm{Da}_l c_g \text{ in } V_g, \tag{86}$$

$$c_f=c_g \text{ on } \Sigma=0, \tag{87}$$

$$\boldsymbol{\nabla}c_f\cdot\mathbf{n}=D_g\boldsymbol{\nabla}c_g\cdot\mathbf{n} \text{ on } \Sigma=0. \tag{88}$$

We now use the multiple scales technique, as for the fluid problem, and introduce independent local and global lengthscales $\mathbf{X}$ and $\mathbf{x}$ related to each other through $\mathbf{x}=\varepsilon\mathbf{X}$. Expanding the gradient and laplacian operators through (49) gives

$$\varepsilon\overline{\mathrm{Pe}_l}\left(\varepsilon\frac{\partial c_f}{\partial t}+\mathbf{u}\cdot\boldsymbol{\nabla}_X c_f+\varepsilon\mathbf{u}\cdot\boldsymbol{\nabla}_x c_f\right)=\nabla_X^2 c_f+2\varepsilon\boldsymbol{\nabla}_x\cdot\boldsymbol{\nabla}_X c_f+\varepsilon^2\nabla_x^2 c_f \text{ in } V_f, \tag{89}$$

$$\varepsilon^2\overline{\mathrm{Pe}_l}\frac{\partial c_g}{\partial t}=D_g\nabla_X^2 c_g+2\varepsilon D_g\boldsymbol{\nabla}_x\cdot\boldsymbol{\nabla}_X c_g+\varepsilon^2 D_g\nabla_x^2 c_g - \mathrm{Da}_l c_g \text{ in } V_g, \tag{90}$$

$$c_f=c_g \text{ on } \Sigma_\varepsilon=0, \tag{91}$$

$$\boldsymbol{\nabla}_X c_f\cdot\mathbf{n}+\varepsilon\boldsymbol{\nabla}_x c_f\cdot\mathbf{n}=D_g\boldsymbol{\nabla}_X c_g\cdot\mathbf{n}+\varepsilon D_g\boldsymbol{\nabla}_x c_g\cdot\mathbf{n} \text{ on } \Sigma_\varepsilon=0. \tag{92}$$

We now consider the different cases in turn.

$\underline{\mathrm{Da}_l=\mathcal{O}\left(\varepsilon^2\right)}$ In this case we let $\mathrm{Da}_l=\varepsilon^2\overline{\mathrm{Da}}$ where $\overline{\mathrm{Da}}=\mathcal{O}(1)$. We expand $\mathbf{u}$ in powers of ε as in (53) and c_f and c_g as

$$c_f=c_f^{(0)}(\mathbf{x},\mathbf{X},t)+\varepsilon c_f^{(1)}(\mathbf{x},\mathbf{X},t)+\dots, \tag{93}$$

$$c_g=c_g^{(0)}(\mathbf{x},\mathbf{X},t)+\varepsilon c_g^{(1)}(\mathbf{x},\mathbf{X},t)+\dots, \tag{94}$$

where $c_f^{(j)}$ and $c_g^{(j)}$ are assumed to be periodic in $\mathbf{X}$. Equating powers of ε^0 yields

$$\nabla_X^2 c_f^{(0)}=0 \text{ in } V_f, \tag{95}$$

$$D_g\nabla_X^2 c_g^{(0)}=0 \text{ in } V_g, \tag{96}$$

$$c_f^{(0)}=c_g^{(0)} \text{ on } \Sigma_\varepsilon=0, \tag{97}$$

$$\boldsymbol{\nabla}_X c_f^{(0)}\cdot\mathbf{n}=D_g\boldsymbol{\nabla}_X c_g^{(0)}\cdot\mathbf{n} \text{ on } \Sigma_\varepsilon=0. \tag{98}$$

The only possible solution of this system is that both $c_f^{(0)}$ and $c_g^{(0)}$ are constant on the local scale and so given by $c_f^{(0)}=c_g^{(0)}=\overline{c}(\mathbf{x},t)$ where $\overline{c}(\mathbf{x},t)$ is to be determined from a homogenized equation. Equating powers of ε in (89)-(92) and noting that $\overline{c}$ is

independent of the local variable $\mathbf{X}$ gives

$$\nabla_X^2 c_f^{(1)} = 0 \text{ in } V_f, \tag{99}$$

$$D_g \nabla_X^2 c_g^{(1)} = 0 \text{ in } V_g, \tag{100}$$

$$c_f^{(1)} = c_g^{(1)} \text{ on } \Sigma_\varepsilon = 0, \tag{101}$$

$$\boldsymbol{\nabla}_X c_f^{(1)} \cdot \mathbf{n} = D_g \boldsymbol{\nabla}_X c_g^{(1)} \cdot \mathbf{n} + (D_g - 1)\, \boldsymbol{\nabla}_x \overline{c} \text{ on } \Sigma_\varepsilon = 0. \tag{102}$$

Again, this system only admits solutions where both $c_f^{(1)}$ and $c_g^{(1)}$ are constant on the local scale so given by $c_f^{(1)} = c_g^{(1)} = \overline{c}^{(1)}(\mathbf{x}, t)$ where $\overline{c}^{(1)}(\mathbf{x}, t)$ could be determined. Finally, equating powers of ε^2 gives the homogenized transport equation for $\overline{c}$. The $\mathcal{O}\left(\varepsilon^2\right)$ system gives

$$\nabla_X^2 c_f^{(2)} + \nabla_x^2 \overline{c} = \overline{\mathrm{Pe}_l} \frac{\partial \overline{c}}{\partial t} + \overline{\mathrm{Pe}} \mathbf{u}^{(0)} \cdot \boldsymbol{\nabla}_x \overline{c} \text{ in } V_f, \tag{103}$$

$$\nabla_X^2 c_g^{(2)} + D_g \nabla_x^2 \overline{c} = \overline{\mathrm{Pe}_l} \frac{\partial \overline{c}}{\partial t} + \overline{\mathrm{Da}} \overline{c} \text{ in } V_g, \tag{104}$$

$$c_f^{(2)} = c_g^{(2)} \text{ on } \Sigma_\varepsilon = 0\ , \tag{105}$$

$$\boldsymbol{\nabla}_X c_f^{(2)} \cdot \mathbf{n} - D_g \boldsymbol{\nabla}_X c_g^{(2)} \cdot \mathbf{n} = (D_g - 1)\, \boldsymbol{\nabla}_x \overline{c}^{(1)} \cdot \mathbf{n} \text{ on } \Sigma_\varepsilon = 0\ . \tag{106}$$

We integrate this system over the periodic cell V to derive the transport equation for $\overline{c}$. Using the Divergence Theorem, periodicity, defining $\mathbf{n}$ as the unit normal pointing into the gel and noting that $\overline{c}(\mathbf{x}, t)$ is independent of the local variable $\mathbf{X}$ gives

$$\begin{aligned}\iint_{\Sigma_\varepsilon = 0} \left(\boldsymbol{\nabla}_X c_f^{(2)} - D_g \boldsymbol{\nabla}_X c_g^{(2)} \right) \cdot \mathbf{n} \mathrm{d}S =& \overline{\mathrm{Pe}_l} \left(|V_f| + |V_g| \right) \frac{\partial \overline{c}}{\partial t} + \overline{\mathrm{Pe}_l} \, |V| \, \langle \mathbf{u}^{(0)} \rangle \cdot \boldsymbol{\nabla}_x \overline{c} \\ &+ \overline{\mathrm{Da}} \, |V_g| \, \overline{c} - \left(|V_f| + D_g \, |V_g| \right) \nabla_x^2 \overline{c}. \end{aligned} \tag{107}$$

However, using the boundary condition (106) and noting that $\overline{c}^{(1)} = \overline{c}^{(1)}(\mathbf{x}, t)$ it is clear that the LHS of (107) is zero and so the average concentration $\overline{c}$ evolves according to

$$\boxed{\overline{\mathrm{Pe}_l} \left(\frac{\partial \overline{c}}{\partial t} + \langle \mathbf{u}^{(0)} \rangle \cdot \boldsymbol{\nabla}_x \overline{c} \right) = K \nabla_x^2 \overline{c} - \overline{\mathrm{Da}}\ n_g\ \overline{c},} \tag{108}$$

where the diffusion coefficient is given by

$$K = n_f + D_g n_g \tag{109}$$

and

$$n_f = \frac{|V_f|}{|V|}\ ,\ n_g = \frac{|V_g|}{|V|}. \tag{110}$$

From (108) it is clear that the average concentration $\overline{c}$ advects with the average fluid velocity $\langle \mathbf{u}^{(0)} \rangle$, diffuses with coefficient K and reacts with coefficient $\overline{\mathrm{Da}}\ n_g$. Equation (108) should be solved in the construct subject to an appropriate initial condition

$$\overline{c}(\mathbf{x}, 0) = c_{in}(\mathbf{x})\,. \tag{111}$$

$\underline{\mathrm{Da}_l = \mathcal{O}\left(\varepsilon^3\right) \textbf{ and smaller}}$ In this case we let $\mathrm{Da}_l = \varepsilon^3\overline{\mathrm{Da}}$ where $\overline{\mathrm{Da}} = \mathcal{O}(1)$. The analysis for this is identical to the case when $\mathrm{Da}_l = \mathcal{O}\left(\varepsilon^2\right)$ until we equate powers of ε^2, and so (95) - (102) remain unchanged. Now, as $\mathrm{Da}_l = \mathcal{O}\left(\varepsilon^3\right)$ no reaction term features in the $\mathcal{O}\left(\varepsilon^2\right)$ system which determines the homogenized transport equation for $\overline{c}$. Equating powers of ε^2 now gives

$$\nabla_X^2 c_f^{(2)} + \nabla_x^2 \overline{c} = \overline{\mathrm{Pe}_l}\frac{\partial \overline{c}}{\partial t} + \overline{\mathrm{Pe}}\mathbf{u}^{(0)} \cdot \boldsymbol{\nabla}_x \overline{c} \text{ in } V_f, \tag{112}$$

$$\nabla_X^2 c_g^{(2)} + D_g \nabla_x^2 \overline{c} = \overline{\mathrm{Pe}_l}\frac{\partial \overline{c}}{\partial t} \text{ in } V_g, \tag{113}$$

$$c_f^{(2)} = c_g^{(2)} \text{ on } \Sigma_\varepsilon = 0\ , \tag{114}$$

$$\boldsymbol{\nabla}_X c_f^{(2)} \cdot \mathbf{n} - D_g \boldsymbol{\nabla}_X c_g^{(2)} \cdot \mathbf{n} = (D_g - 1)\,\boldsymbol{\nabla}_x \overline{c}^{(1)} \cdot \mathbf{n} \text{ on } \Sigma_\varepsilon = 0\ , \tag{115}$$

and so the average oxygen concentration $\overline{c}$ evolves according to

$$\boxed{\overline{\mathrm{Pe}_l}\left(\frac{\partial \overline{c}}{\partial t} + \langle \mathbf{u}^{(0)} \rangle \cdot \boldsymbol{\nabla}_x \overline{c}\right) = K \nabla_x^2 \overline{c}.} \tag{116}$$

Therefore $\overline{c}$ advects with the average fluid velocity $\langle \mathbf{u}^{(0)} \rangle$ and diffuses with coefficient K. Again, (116) should be solved subject to an appropriate initial condition such as (111).

5.2.4 Numerical Results : Oxygen

We used *COMSOL Multiphysics* to solve the PDEs (108) and (116) for typical parameter values subject to the initial condition $\overline{c}(\mathbf{x}, 0) = 0$ and boundary condition $\overline{c} = 1$ on the 'source' face of the structure (so on the left curved section of the cylinder for Figures (20), (21) and on the top circular face for Figures (22), (23)). Firstly the results show the difference between the cases $\mathrm{Da}_l = \mathcal{O}\left(\varepsilon^2\right)$ and $\mathrm{Da}_l = \mathcal{O}\left(\varepsilon^3\right)$ (compare Figures (20), (21) or (22), (23)). Clearly when this reaction term is larger, the concentrations of oxygen through the construct are smaller. Also, the results show the benefit of directing the fluid through the top of the construct as compared to the side as the concentration values are smaller in Figures (20), (21) compared to (22), (23).

5.2.5 Conclusions on Homogenization

The homogenization approach is a flexible mathematical technique for investigating this system. Analysis of the fluid yields the permeability tensor for the structure. Analysis of the oxygen system gave an upper bound on the cell density in the gel and showed that it is beneficial to direct the fluid through the top of the construct as opposed to the side. It also gave a clear understanding of the transport properties of oxygen on both the local and global lengthscales. The approach would be particularly useful to investigate lactate transport, and this will be discussed next.

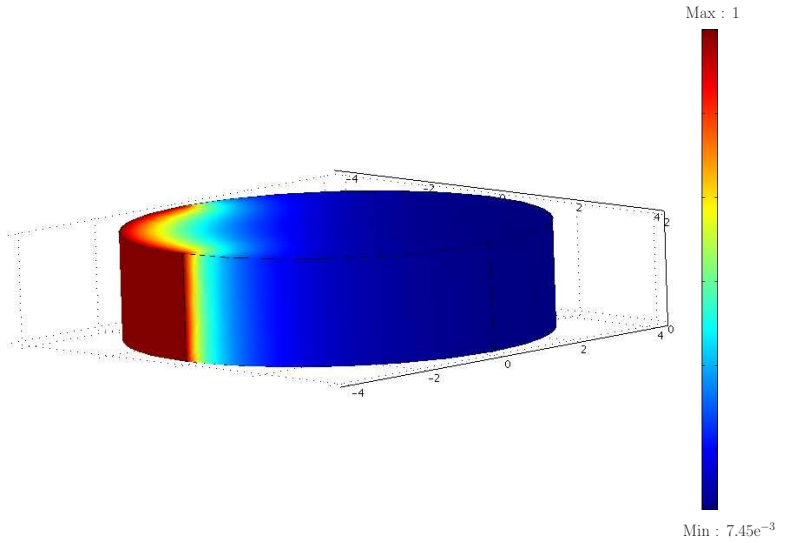

Figure 20: Case $\mathrm{Da}_l = \mathcal{O}\left(\varepsilon^2\right)$. Solution of (108) with local structure (15), $\overline{\mathrm{Pe}} = 1.125$, $\overline{\mathrm{Da}} = 1$, $t = 10$ when the fluid is directed through the left side of the construct

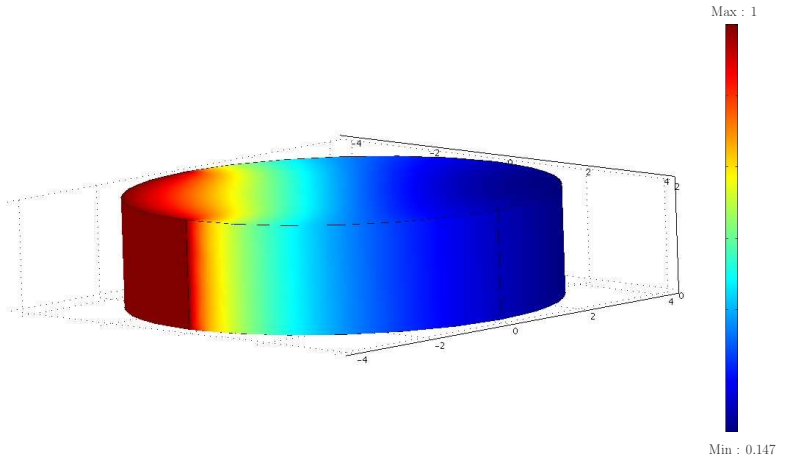

Figure 21: Case $\mathrm{Da}_l = \mathcal{O}\left(\varepsilon^3\right)$. Solution of (116) with local structure (15), $\overline{\mathrm{Pe}} = 1.125$, $t = 10$ when the fluid is directed through the left side of the construct

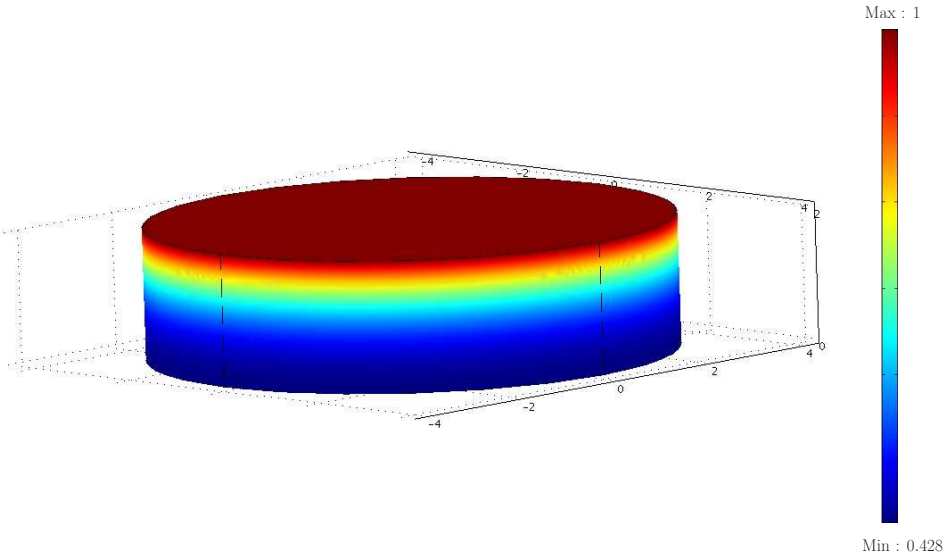

Figure 22: Case $\mathrm{Da}_l = \mathcal{O}\left(\varepsilon^2\right)$. Solution of (108) with local structure (15), $\overline{\mathrm{Pe}} = 1.125$, $\overline{\mathrm{Da}} = 1$, $t = 10$ when the fluid is directed through the top of the construct

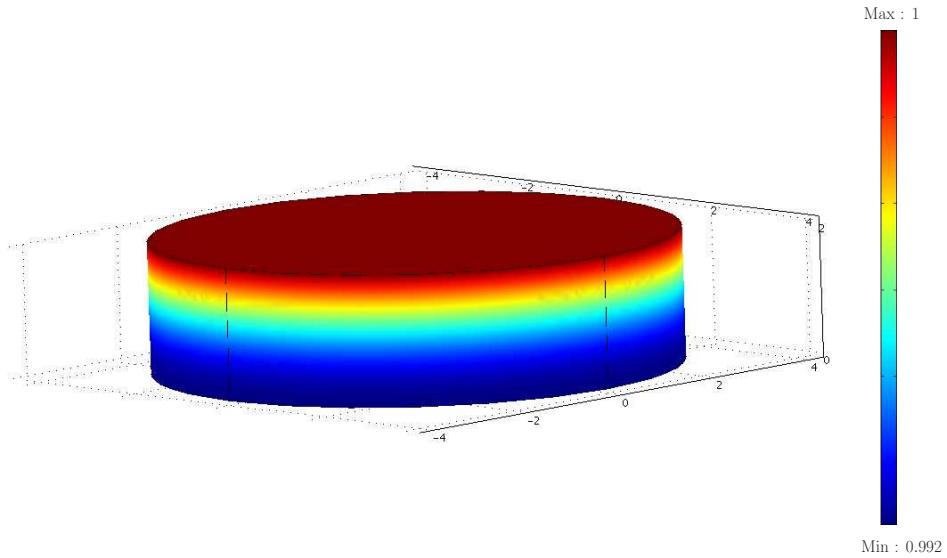

Figure 23: Case $\mathrm{Da}_l = \mathcal{O}\left(\varepsilon^3\right)$. Solution of (116) with local structure (15), $\overline{\mathrm{Pe}} = 1.125$, $t = 10$ when the fluid is directed through the top of the construct

5.3 Further Work - Homogenization Problem for Lactate and when Cell Density Varies on the Global Scale

The obvious next step is to extend the homogenization approach to analyse lactate transport, however to do this we need a full understanding of the system. The published data on diffusion coefficients for lactate is inconsistent, and some sources have them of the same order of magnitude as oxygen (note that in this case there would be no point in producing a scaffold for the purposes of waste product removal, see §5.1). More investigation should be carried out to check the values used in this report. Lactate is produced when lactic acid dissociates into lactate and hydrogen ions H^+, and so increased lactate levels are taken to be an indicator of increased acidity of the medium. This decrease in pH prohibits the proliferation of cells which is why lactate must be removed. However, this is complicated by two main factors. Firstly, lactate is in general understood to be a waste product of anaerobic respiration and this would indicate that lactate concentration should increase with decreasing oxygen concentration. However, this is not necessarily correct as demonstrated by Figure (24) from [9], where increasing oxygen concentration is shown to increase lactate production. Therefore, in order to model the lactate transport effectively we first need to develop a clear understanding of the reaction schemes that produce it. A second consideration is that the fluid contains a buffer solution which helps to prevent pH changes and so any model for lactate transport must include the effect of this buffering on the system. Finally, lactate is not the only source of hydrogen ions H^+ in the system. For example, carbon dioxide is produced as a waste product of aerobic respiration and is also acidic. Instead of purely focussing on lactate production and transport, we should really consider all sources of H^+ and to this we need the data for all of the relevant reaction schemes.

It is also important to extend the current analysis to the case when the cell density ϕ varies as a function of the global variables $\mathbf{x}$. The setup would then compare to the setup shown in Figure (2).

Hopefully we will be able to consider both of these extensions in follow-up meetings.

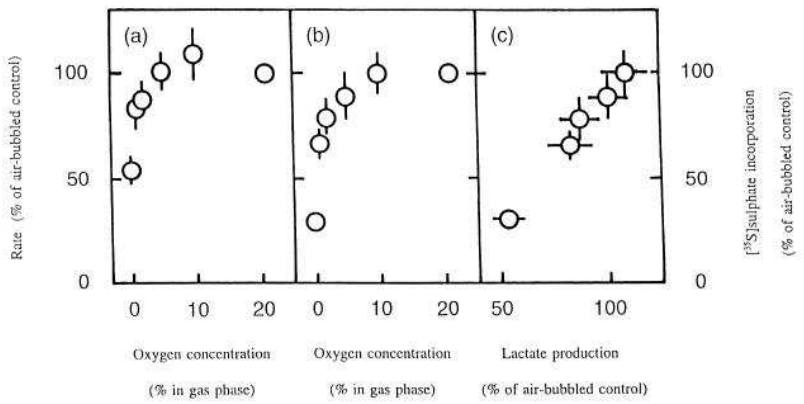

Figure 24: Effect of oxygen concentration on (a) lactate production, (b) $\left[^{35}\mathrm{S}\right]$sulphate incorporation, by bovine articular cartilage; and (c) relationship between lactate production and $\left[^{35}\mathrm{S}\right]$sulphate incorporation in the same sample of cartilage. Reproduced from [9]

References

[1] M. Ahearne, Y. Yang, A.J. El Haj, K.Y. Then, and K.K. Liu. Characterizing the viscoelastic properties of thin hydrogel-based constructs for tissue engineering applications. *J. R. Soc.*, 2005.

[2] C. Bailey, R. Booth, S. Cartmell, L. P. Chini, L. Cummings, R. Dyson, V. Michael, S. Naire, S. Payvandi, Z. Rong, S. Waters, R. Whittaker, and H. Woollard. Optimisation of fluid distribution inside a porous construct. *Proceedings of the 6th Mathematics in Medicine Study Group*, 2006.

[3] J. T. Borenstein, H. Terai, E. J. King, K. R. adn Weinberg, M. R. Kaazempur-Mofrad, and J. P. Vacanti. Microfabrication technology for vascularized tissue engineering. *Biomedical Microdevices*, 2002.

[4] M. A. Dimicco and R. L. Sah. Dependence of cartilage matrix composition on biosynthesis, diffusion, and reaction. *Transport In Porous Media*, 50:57–73, 2003.

[5] Mouw J.K., N.D. Case, R. E. Guldberg, A. H. K. Plaas, and M. E. Levenston. Variations in matrix composition and GAG fine structure among scaffolds for cartilage tissue engineering. *OsteoArthritis and Cartilage*, 13:828–836, 2005.

[6] M. R. Kaazempur-Mofrad, J. T. Borenstein, L. M. Hartman, W. S. Cheung, E. J. Weinberg, M. Shin, A. Sevy, and J. P. Vacanti. Vascularized tissue engineering of vital organs : Design, modelling and functional testing.

[7] D.L. Koch and A.J.C. Ladd. Moderate reynolds number flows through periodic and random arrays of aligned cylinders. *J. Fluid Mech.*, 1997.

[8] C.S.D. Lee, J.P. Gleghorn, N.W. Choi, M. Cabodi, A.D. Stroock, and L.J. Bonassar. Integration of layered chondrocyte-seeded alginate hydrogel scaffolds. *Biomat.*, 2007.

[9] R. B. Lee and J. P. G. Urban. Evidence for a negative Pasteur effect in articular cartilage. *Biochem. J.*, 321:95–102, 1997.

[10] J. Malda. *Cartilage tissue engineering : The relevance of oxygen.* PhD thesis, Twente University, 2003.

[11] J. Malda, T. B. F. Woodfield, F. van der Vloodt, C. Wilson, D. E. Martens, J. Tramper, C. A. van Blitterswijk, and Riesle. J. The effect of PEGT/PBT scaffold architecture on the composition of tissue engineered cartilage. *Biomaterials*, 2005.

[12] G. A. Pavliotis and A. M. Stuart. Multiscale methods: Averaging and homogenization. Lecture notes accompanying LMS-EPSRC short course on multiscale methods, February 2007.

[13] Thomas M. Quinn, Alan J. Grodzinsky, Michael D. Buschmann, Young-Jo Kim, and Ernst B. Hunziker. Mechanical compression alters proteoglycan deposition and matrix deformation around individual cells in cartilage explants. *J. Cell Science*, 111:573–583, 1998.

[14] B. G. Sengers, C. W. J. Oomens, and F. P. T. Baaijens. An integrated finite-element approach to mechanics, transport and biosynthesis in tissue engineering. *J. Biomech. Eng.-Trans. ASME*, 126(1):82 – 91, 2004.